Spatial and Temporal Shape Constrained Deformable Surfaces for 3D and 4D Medical Image Segmentation

Johan Montagnat, Hervé Delingette

INRIA

INSTITUT NATIONAL DE RECHERCHE EN INFORMATIQUE ET EN AUTOMATIQUE

Spatial and temporal shape constrained deformable surfaces for 3D and 4D medical image segmentation

Johan Montagnat — Hervé Delingette

N° 4078

November 2000

THÈME 3

ISSN 0249-6399 ISRN INRIA/RR--4078--FR+ENG

INRIA
SOPHIA ANTIPOLIS

Spatial and temporal shape constrained deformable surfaces for 3D and 4D medical image segmentation

Johan Montagnat , Hervé Delingette

Thème 3 — Interaction homme-machine,
images, données, connaissances
Projet Epidaure

Rapport de recherche n° 4078 — November 2000 — 70 pages

Abstract: Segmentation remains one of the main problem of image analysis. In particular, 3D medical image segmentation is difficult due to noise, low contrast and outliers resulting from any 3D imaging technologies. However, image segmentation is a first step required for quantitative measurements, automatic diagnosis and modelling of anatomical structures in medical images. Due to the complex shape of anatomical structures and the large inter-patient shape variability, powerful modelling tools are required. In this report, we describe a segmentation tool based on deformable surfaces well suited to the shape reconstruction and modelling of anatomical structures from 3D medical images. The deformable surfaces are based on discrete meshes that can represent manifolds without any topology restrictions. These meshes rely on shape constraints at local and global scale for introducing prior knowledge on the structures to segment and for regularizing the surface deformations. Different data terms are proposed to cover reconstruction from different imaging modalities.

Time sequence of 3D images, or 4D images, are commonly used for heart motion analysis and cardiac pathologies diagnosis. In this paper, we extend the deformable surface reconstruction framework to the 4D case. In particular, we introduce temporal constraints to regularize deformations in the time dimension. Prior knowledge on the heart motion is introduced through trajectory constraints that are complementary to spatial constraints. Segmentation of the heart left ventricle in different imaging modalities is demonstrated.

Key-words: Deformable Surface, shape, 3D, 4D, medical images, image teMporal Sequence, heart

Unité de recherche INRIA Sophia Antipolis
2004, route des Lucioles, B.P. 93, 06902 Sophia Antipolis Cedex (France)
Téléphone : 04 92 38 77 77 - International : +33 4 92 38 77 77 — Fax : 04 92 38 77 65 - International : +33 4 92 38 77 65

Contraintes de forme spatiales et temporelles de surfaces déformables pour la segmentation d'images médicales 3D et 4D.

Résumé : La segmentation demeure l'un des problèmes principaux de l'analyse d'images. En particulier, la segmentation d'images médicales 3D est rendue difficile par la présence de bruit, le faible contraste et les point aberrants inhérents à toutes les modalités d'images médicales. La segmentation est néanmoins une étape nécessaire à l'estimation quantitative de paramètres, au diagnostic automatique et à la modélisation de structures anatomiques dans les images médicales. La forme complexe des structures anatomiques et l'importante variabilité de la forme des organes d'un patient à l'autre renforce le besoin d'outils de modélisation puissants. Dans ce rapport, nous décrivons des surfaces déformables adaptées à la reconstruction et la modélisation de formes 3D de structures anatomiques dans des images médicales 3D. Nous nous concentrons sur une représentation discrète sans limitation topologique. Les maillages utilisés s'appuient sur des contraintes de forme à l'échelle locale et globale pour introduire une connaissance *a priori* des structures à segmenter et pour régulariser le processus de déformation. Différents termes d'attache aux données s'adaptant à différentes modalités d'images sont introduits.

Les séquences temporelles d'images 3D, ou images 4D, sont utilisées en routine pour l'analyse du mouvement cardiaque et le diagnostic des pathologies du cœur. Nous montrons une extension des surfaces déformables au cas 4D. Des contraintes temporelles s'ajoutent au processus de déformation pour introduire une régularization dans la quatrième dimension. Une connaissance *a priori* du mouvement du modèle est introduite par l'intermédiaire de contraintes temporelles de forme qui complètent les contraintes spatiales. Des exemples de segmentation du ventricule gauche sont présentés dans différentes modalités d'images.

Mots-clés : Surface déformable, forme, 3D, 4D, images médicales, séquences temporelles d'images, cœur

1 Context

1.1 4D Medical imagery

One of the major trend in medical imagery in the past few years has been the development of real-time 3D medical imagery. The output of these new imaging modalities is a time series of 3D images, also called 4D medical images. The huge amount of data produced by 3D and 4D acquisition devices make most recent image-based pathology studies intractable by hand.

Image segmentation is a prerequisite for many high-level tasks including medical images analysis, computer-assisted diagnosis or the geometric modelling of anatomical structures. However image segmentation remains one of the main open issues in image analysis because of the poor image quality and low image contrast originating from most imaging devices.

Roughly, segmentation tools may be classified into two broad categories as illustrated in figure 1. Intensity-based approaches extract anatomical structures solely from the image. On the other hand, model based approaches rely additionally on an a priori knowledge of the structures shape to guide the reconstruction process. Both geometric and intensity models of anatomical structures have been proposed in the literature.

1.2 Deformable models based segmentation

In this report we focus on deformable surface based segmentation of 3D and 4D medical images. The main incentive in using deformable models is to introduce knowledge about the shape of the anatomical structures. We are considering surface representations that are well suited to extract organ boundaries in 3D images. Deformable surfaces are composed of a geometric representation and an evolution law governing the surface deformations. This topic has been extensively studied especially for 3D object reconstruction and image segmentation [56, 64].

A deformable surface model is sensitive to noise and outliers of the data to reconstruct. It cannot deform freely and some regularization constraints have to be introduced in the deformation process. Prior information on the data may be introduced by limiting the possible variations of the model to increase the robustness of the segmentation process. Many other complementary ways of relying on prior information have been proposed such as shape statistical variability [23] and intensity of anatomical structures in images [43, 5].

Deformable surfaces produce a geometric representation of the segmented structures. This surface representation is well suited to 3D shape visualization on specialized hardware. With these Geometric models, it is possible to obtain quantitative measures of volume or distances needed for diagnosis and therapy planning. It is also the first step towards the construction of biomechanical models used for surgery simulation [35].

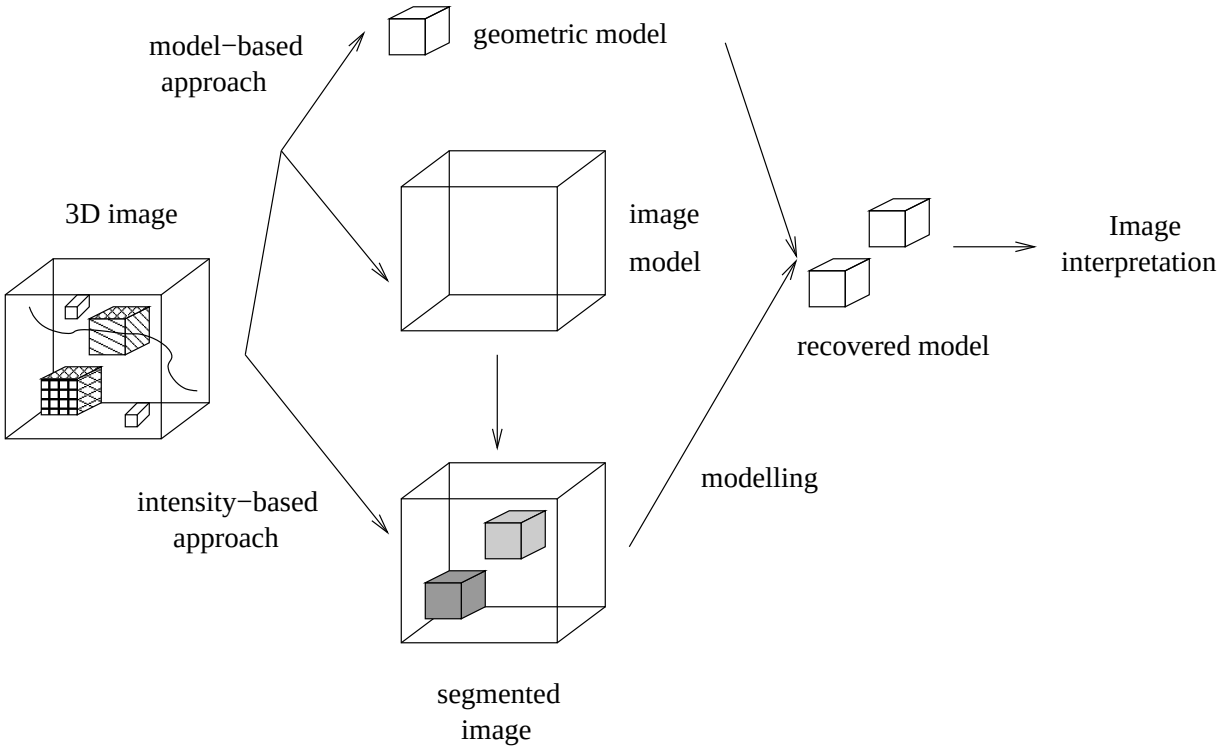

Figure 1: Segmentation: intensity and model based approaches

1.3 4D images segmentation

We address the problem of segmenting time series of 3D medical images. In the remainder, the term 4D images refers to image sequences although the term 3D+T image would be more appropriate. since it emphasizes the different nature of the time dimension. We denote I a 4D image composed of n volume images $\{I_0, \ldots, I_{n-1}\}$ acquired at n different time points $\{t_0, \ldots, t_{n-1}\}$.

An obvious method to segment 4D images is to consider independently every 3D image of the time sequence. The result of the segmentation at instant t may be used as an initialization for segmentation of instant $t+1$ thus taking into account the time continuity only at the initialization of the segmentation process [4, 54]. However, more information on the sequence might be used by considering the whole 4D image.

2 Deformable models

2.1 Surface geometric representation

Let $\mathcal{S}$ represent a deformable surface. $\mathcal{S}$ may have a continuous representation or may be defined as a discrete mesh with a finite set of vertices. Common continuous surfaces used for medical image segmentation are parameterized surfaces [89] such as superquadrics [88] or B-snakes [58], etc [59, 92, 4]. Discrete meshes are defined by a finite set of vertices and a connectivity function between these vertices. Depending on the connectivity function, the mesh might be a triangulation [13], a simplex-mesh [31], a spring-mass model [66], etc.

Among the possible geometric representations of deformable surfaces (see [56] or [64] for a review of surface geometric representations), we have chosen a discrete surface model called *simplex mesh*[31]. Their main advantage lies in their simple data structure permitting an efficient implementation both in terms of computational time and memory storage. This is specifically important in the case of 4D deformable models where n surface meshes must be updated at each iteration. Furthermore, simplex meshes are especially well-suited for the computation of curvature-based regularizing forces.

2.2 Simplex mesh geometry

A surface simplex mesh is defined by a set of d vertices $\{\mathbf{p}_i\}_i \in [0, d-1]$. Each vertex is connected to exactly 3 neighbors. This representation does not restrict the mesh topology and simplex meshes are topologically dual to triangulations. Figure 2 diagrams a surface simplex mesh example (solid line) and its dual triangulation (dashed line).

The main feature of simplex meshes lies in their simple geometric description. Figure 3 diagrams a vertex $\mathbf{p}_i$ of a simplex mesh and its three neighbors, $\mathbf{p}_{\mathrm{ngh}_j(i)}, j \in \{1,2,3\}$. Let $\mathcal{P}_i$ be the plane defined by $\mathbf{p}_i$'s three neighbors. We denote $\mathbf{p}_i^\perp$ the projection of $\mathbf{p}_i$ on $\mathcal{P}_i$ and $\mathbf{n}_i$ the unit normal vector of $\mathcal{P}_i$. We introduce the circumscribed circle to triangle $(\mathbf{p}_{\mathrm{ngh}_1(i)}, \mathbf{p}_{\mathrm{ngh}_2(i)}, \mathbf{p}_{\mathrm{ngh}_3(i)})$ with centre $\mathbf{c}_i$ and radius r_i, and the circumscribed sphere to vertices $(\mathbf{p}_i, \mathbf{p}_{\mathrm{ngh}_1(i)}, \mathbf{p}_{\mathrm{ngh}_2(i)}, \mathbf{p}_{\mathrm{ngh}_3(i)})$ with centre $\mathbf{o}_i$ and radius R_i.

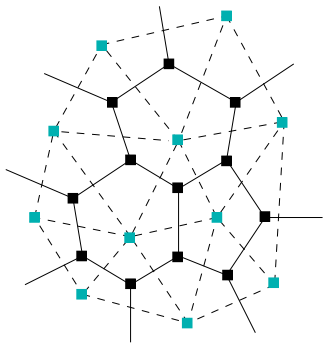

Figure 2: Surface simplex mesh duality with triangulations.

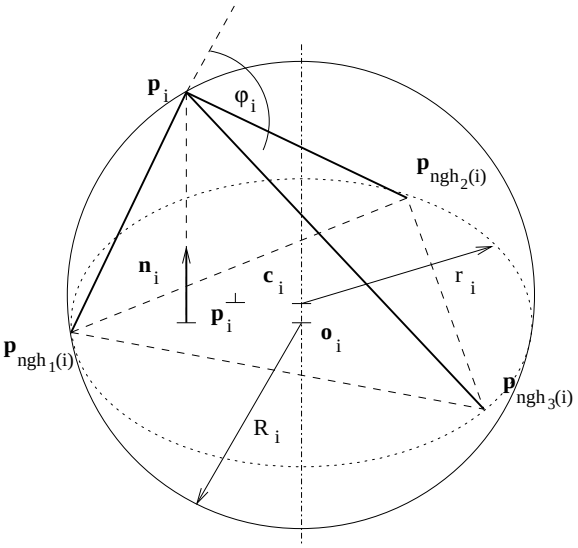

Figure 3: Simplex mesh geometry.

We call *metric parameters* the barycentric coordinates ε_i^1, ε_i^2, and $\varepsilon_i^3 = 1 - \varepsilon_i^1 - \varepsilon_i^2$ of $\mathbf{p}_i^\perp$ with respect to $\mathbf{p}_i$'s neighbors. They control the relative position of $\mathbf{p}_i^\perp$ in $\mathcal{P}_i$:

$$\mathbf{p}_i^\perp = \sum_{j=1}^{3} \varepsilon_i^j \mathbf{p}_{\mathrm{ngh}_j(i)}$$

The *simplex angle* $\varphi_i \in [-\pi, \pi]$ is defined by :

$$\begin{cases} \sin(\varphi_i) = \frac{r_i}{R_i} \mathrm{sign}((\mathbf{p}_{\mathrm{ngh}_1(i)} - \mathbf{p}_i) \cdot \mathbf{n}_i) \\ \cos(\varphi_i) = \frac{\|\mathbf{c}_i - \mathbf{o}_i\|}{R_i} \mathrm{sign}((\mathbf{c}_i - \mathbf{o}_i) \cdot \mathbf{n}_i). \end{cases}$$

It controls the elevation of vertex $\mathbf{p}_i$ above $\mathcal{P}_i$. We define a vertex discrete mean curvature as $H_i = \frac{1}{R_i} = \frac{\sin(\varphi_i)}{r_i}$. Under some assumptions it can be shown [30] that the discrete curvature of a mesh whose vertices lie on a continuous and sufficiently differentiable surface converges towards the surface mean curvature at the vertex position.

The vertex position $\mathbf{p}_i$ is uniquely defined by its three neighbors, its metric parameters and its simplex angle :

$$\mathbf{p}_i = \left(\sum_{j=1}^{3} \varepsilon_i^j \mathbf{p}_{\mathrm{ngh}_j(i)} \right) + h(\mathbf{p}_{\mathrm{ngh}_j(i)}, \varepsilon_i^j, \varphi_i)\mathbf{n}_i.$$

where:

$$h = \frac{(r_i^2 - d_i^2)tan(\varphi_i)}{\epsilon\sqrt{r_i^2 + (r_i^2 - d_i^2)tan(\varphi_i)^2} + r_i}, \tag{1}$$

$$\epsilon = \begin{cases} 1 \text{ if } |\varphi_i| < \frac{\pi}{2} \\ -1 \text{ if } |\varphi_i| > \frac{\pi}{2} \end{cases}, \quad d_i = \|\mathbf{p}_i^\perp \mathbf{c}_i\|.$$

It can be shown [30] that a simplex mesh shape is defined up to a similarity transformation by the set of its metric parameters and simplex angles $\{\varepsilon_i^1, \varepsilon_i^2, \varphi_i\}_i$.

2.3 Surface law of motion

A surface deforms under the combined action of a regularization, or internal, term enforcing some level of smoothness and a data, or external, term enforcing the convergence of the surface towards the data. In this paper we consider a second order (Newtonian) evolution framework:

$$\mathbf{M}\frac{\partial^2 \mathcal{S}}{\partial \tau^2} + \mathbf{C}\frac{\partial \mathcal{S}}{\partial \tau} + \mathbf{K}(\mathcal{S}) = \mathbf{f}(\mathcal{S}), \tag{2}$$

where $\mathbf{M}$, $\mathbf{C}$, and $\mathbf{K}$ are the model mass, damping, and stiffness matrices respectively. In this equation τ designates a temporal variable describing the time necessary for an initial

model to converge towards its final shape. The model evolution time τ is clearly distinct from the temporal variable $\mathbf{t}$ corresponding to the physical time of image acquisition.

For discrete meshes, the $\mathbf{M}$, $\mathbf{C}$, and $\mathbf{K}$ matrices are diagonal. Equation 2 rewrites:

$$m(i)\frac{d^2\mathbf{p}_i}{d\tau^2} + \gamma\frac{d\mathbf{p}_i}{d\tau} - \alpha(i)f_{\text{int}}(\mathbf{p}_i) = \beta(i)f_{\text{ext}}(\mathbf{p}_i), \tag{3}$$

where:

- $m(i)$ is the i^{th} vertex mass;
- γ is the background damping;
- f_{int} is the regularizing force;
- f_{ext} is the data force;
- $\alpha(i)$ and $\beta(i)$ are two weights controlling the internal and external terms.

This equation corresponds to an equilibrium between the inertial force, the regularizing force and the data force. Equation 3 has to be discretized in time τ. We consider an explicit scheme discretization leading to equation:

$$\mathbf{p}_i^{\tau+\Delta\tau} = \mathbf{p}_i^{\tau} + \left(1 - \frac{\gamma(i)\Delta\tau}{m(i)}\right)(\mathbf{p}_i^{\tau} - \mathbf{p}_i^{\tau-\Delta\tau}) + \frac{\Delta\tau^2}{m(i)}\left(\alpha(i)f_{\text{int}}(\mathbf{p}_i^{\tau}) + \beta(i)f_{\text{ext}}(\mathbf{p}_i^{\tau})\right).$$

which rewrites as:

$$\mathbf{p}_i^{\tau+\Delta\tau} = \mathbf{p}_i^{\tau} + (1-\gamma)(\mathbf{p}_i^{\tau} - \mathbf{p}_i^{\tau-\Delta\tau}) + \alpha_i f_{\text{int}}(\mathbf{p}_i^{\tau}) + \beta_i f_{\text{ext}}(\mathbf{p}_i^{\tau}), \tag{4}$$

where α_i and β_i are force weights including the vertex mass and the time step. The stability of this scheme is guaranteed if α_i, β_i, and γ range inside given bounds [60]. In all our experiments, γ is fixed to value 0.35 based on an empirical study showing that this value optimizes the convergence speed in general. The α value is always fixed to 1 and only the β coefficient is used to weight the forces equilibrium.

2.4 4D deformable models

To deal with 4D (3D+T) images, we propose to use 4D deformable models as a set of shapes through time. Thus, a 4D model $\mathcal{S}$ is composed by a set of n 3D deformable models $\{\mathcal{S}_t\}_{t\in[0,n-1]}$. As illustrated in figure 4, all n surface meshes $\mathcal{S}_t$ have the same topology, i.e. there is a one to one correspondence between the d vertices composing each surface. In the rest of the paper, $\mathbf{p}_{i,t}$ denotes the position of vertex number i at time t.

While the model undergoes deformations, each surface $\mathcal{S}_t$ evolves in space but it remains at its time position (i.e., a vertex undergoes deformations in 3D space, t does not change). The choice of having meshes of the same topology over time is governed by the goal of efficiency and implementation simplicity. Our approach could be generalized to handle different topologies over time at the expense of additional computational cost. However, for the different applications we have investigated, this need for greater modeling complexity did not appear.

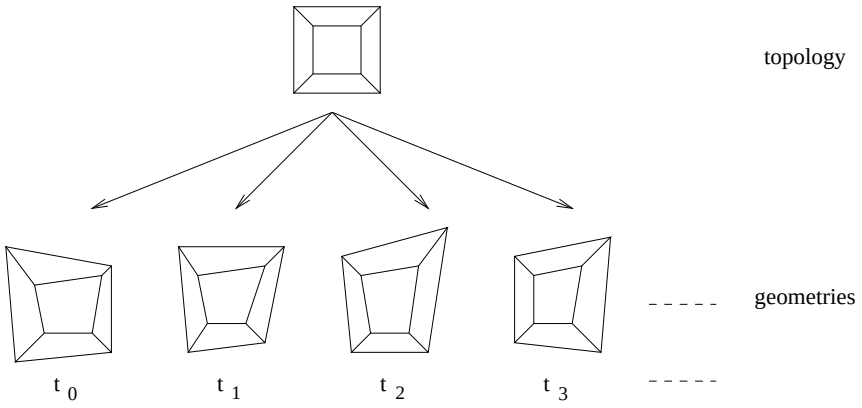

Figure 4: Example of a 4D deformable simplex mesh : there is a one-to-one correspondence between vertices over time.

2.4.1 4D meshes geometry

The set $\{\mathbf{p}_{i,t}\}_{t\in[0,n-1]}$ represents the *trajectory* of the vertex number i along time. It is important to note that the trajectory $\{\mathbf{p}_{i,t}\}_t$ of a vertex does not correspond to the trajectory of physical points of the recovered anatomical structures. Trajectories are only used as a mathematical support to compute temporal constraints but they provide no clues as to the physical motion of the anatomical structure through time.

Figure 5 illustrates the elements composing the vertex trajectories geometry. From a geometrical point of view trajectory $\{\mathbf{p}_{i,t}\}_t$ represents a discrete line in $\mathbb{R}^3$. Each vertex $\mathbf{p}_{i,t}$ owns two temporal neighbors defined by the position of the vertex at the previous and following instant, $\mathbf{p}_{i,t-1}$ and $\mathbf{p}_{i,t+1}$. We consider that trajectories are closed and each vertex owns exactly two neighbors *i.e.* $p_{i,-1} = p_{i,n-1}$ and $p_{i,n} = p_{i,0}$.

Let $\mathbf{p}_{i,t}^{\perp}$ denote the orthogonal projection of $\mathbf{p}_{i,t}$ onto segment $[\mathbf{p}_{i,t-1}, \mathbf{p}_{i,t+1}]$. The position of point $\mathbf{p}_{i,t}$ relatively to its temporal neighbors may be defined through three geometric parameters:

- a metric parameter $\varepsilon_{i,t}$ measuring the relative position of $\mathbf{p}_{i,t}^{\perp}$ in $[\mathbf{p}_{i,t-1}, \mathbf{p}_{i,t+1}]$ ($\mathbf{p}_{i,t}^{\perp} = \varepsilon_{i,t}\mathbf{p}_{i,t-1} + (1-\varepsilon_{i,t})\mathbf{p}_{i,t+1}$);
- an angle $\varphi_{i,t}$ measuring the elevation of $\mathbf{p}_{i,t}$ above the segment $[\mathbf{p}_{i,t-1}, \mathbf{p}_{i,t+1}]$ in plane $(\mathbf{p}_{i,t-1}, \mathbf{p}_{i,t}, \mathbf{p}_{i,t+1})$;
- an angle $\psi_{i,t}$ measuring the discrete torsion of the trajectory.

Intuitively, $\varepsilon_{i,t}$, $\varphi_{i,t}$, and $\psi_{i,t}$ correspond to discrete arc length, curvature, and torsion respectively. Let $\mathbf{t}_{i,t}$ denote the discrete tangent, $\mathbf{b}_{i,t}$ the binormal vector, and $\mathbf{n}_{i,t}$ the

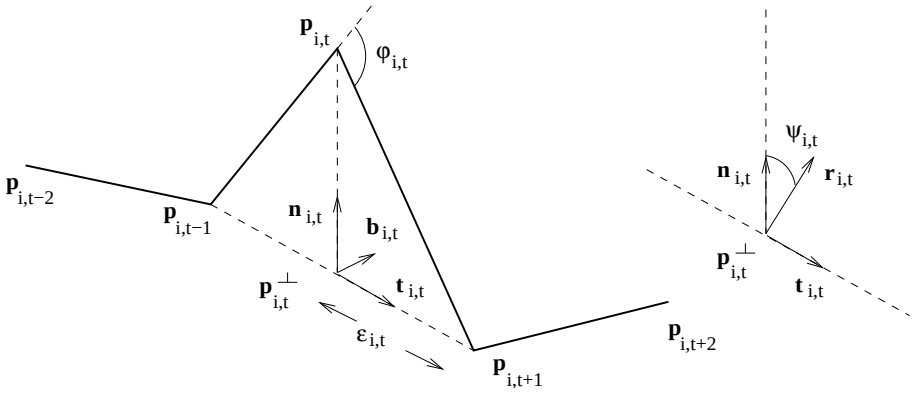

Figure 5: Trajectory geometry.

discrete normal to point $\mathbf{p}_{i,t}$ respectively:

$$\mathbf{t}_{i,t} = \frac{\mathbf{p}_{i,t-1}\mathbf{p}i,t+1}{\|\mathbf{p}_{i,t-1}\mathbf{p}i,t+1\|},\ \mathbf{b}_{i,t} = \frac{\mathbf{p}_{i,t}\mathbf{p}_{i,t+1} \wedge \mathbf{p}_{i,t-1}\mathbf{p}_{i,t}}{\|\mathbf{p}_{i,t}\mathbf{p}_{i,t+1} \wedge \mathbf{p}_{i,t-1}\mathbf{p}_{i,t}\|},\ \mathbf{n}_{i,t} = \mathbf{b}_{i,t} \wedge \mathbf{t}_{i,t}.$$

The metric parameter is defined by:

$$\varepsilon_{i,t} = \frac{\|\mathbf{p}^{\perp}_{i,t}\mathbf{p}_{i,t+1}\|}{\|\mathbf{p}_{i,t-1}\mathbf{p}_{i,t+1}\|},$$

the elevation angle is:

$$\varphi_{i,t} = (\mathbf{p}_{i,t}\mathbf{p}_{i,t+1}, \mathbf{p}_{i,t-1}\mathbf{p}_{i,t}),$$

and the torsion angle is such that:

$$\mathbf{r}_{i,t} = \frac{\mathbf{t}_{i,t} \wedge (\mathbf{p}_{i,t-2}\mathbf{p}_{i,t-1} \wedge \mathbf{p}_{i,t+1}\mathbf{p}_{i,t+2})}{\|\mathbf{t}_{i,t} \wedge (\mathbf{p}_{i,t-2}\mathbf{p}_{i,t-1} \wedge \mathbf{p}_{i,t+1}\mathbf{p}_{i,t+2})\|} \text{ and } \mathbf{n}_i = \cos(\psi_{i,t})\mathbf{r}_{i,t} + \sin(\psi_{i,t})\mathbf{t}_{i,t} \wedge \mathbf{r}_{i,t}.$$

2.4.2 4D models law of motion

The deformations of a 4D model are computed simultaneously at each instant using an evolution law similar to equation 4. To take into account the time continuity in the image sequence, a new force term, the *temporal force* is added that aims at regularizing the deformations of the surface similarly to the internal force. However, the time force is computed independently from the internal force since the time dimension has very different properties than spatial dimensions in a 4D image: the time dimension might be periodic (case of the cardiac cycle) and the sampling frequency in time is usually very rough compared to the spatial sampling.

Let f_{time} denotes the temporal force. Each 4D model vertex is submitted to the law of motion:

$$\mathbf{p}_{i,t}^{\tau+\Delta\tau} = \mathbf{p}_{i,t}^{t} + \gamma(\mathbf{p}_{i,t}^{\tau} - \mathbf{p}_{i,t}^{\tau-\Delta\tau}) + \alpha_i f_{\text{int}}(\mathbf{p}_{i,t}^{\tau}) + \beta_i f_{\text{ext}}(\mathbf{p}_{i,t}^{\tau}) + \delta_i f_{\text{time}}(\mathbf{p}_{i,t}^{\tau})$$

where δ_i is the weight of the temporal regularization force.

3 Spatial and temporal shape constraints

The main incentive for performing medical image segmentation based on deformable models lies in their ability to incorporate prior knowledge on the structures to recover. In most cases, this knowledge is translated mathematically into a set of regularizing constraints that greatly improves the robustness and accuracy of the segmentation process.

We introduce two complementary constraints that are specifically suited for the model deformation in 4D images. The former consists of a shape constraint that tends to minimize the motion of a 4D mesh through its kinetic energy. The latter is a temporal constraint that relies on prior knowledge about the expected motion of a 4D model. It is important to note that, in contrast to many previous work, both constraints are applied simultaneously thus leading to a true 4D approach.

3.1 Deformation constraints

A deformable model is an elastic surface with many degrees of freedom (DOF). With the evolution law given in section 2.3, the number of DOF directly depends on the number of mesh vertices or the number of discretization points in case of a continuous representations. Indeed, a sufficient number of vertices is required to describe anatomical structures with a high level of details. However, a surface with a high number of DOF deforming freely is very sensitive to the presence of noise and outliers. Therefore, it is necessary to constrain the possible deformations to ensure that important anatomical features (such as high curvature points or other meaningful landmarks) are correctly matched in the deformation process. We rely on a coarse-to-fine approach to achieve this goal: at the coarse level, few DOF should be used to obtain a robust deformation whereas at the finest level, a high number of DOF allows an accurate reconstruction.

Many methods have been proposed in the literature to control the deformation scale of a deformable model. Surface deformation methods can be classified into parameterized deformations and global deformations. Parameterized methods modifies the parameters describing a surface (for instance the 12 parameters of a superquadrics) in order to entail a deformation. Global deformation methods (such as affine transformations) on the other hand, warp the embedding Euclidian space to deform a surface.

Based on parameterized deformations, authors have proposed to control the scale of deformation by combining parameters associated to different scales. For instance, Terzopoulos and Metaxas [88] extend the parameterized representation framework by adding a free deformation term disturbing a superquadric surface. Vemuri and Radisavljevic [92] notice that

it is possible to decompose the additive term on a wavelet basis to provide a continuous transition between highly constrained transformations (involving only the 6 superquadrics parameters) and unconstrained deformations (involving an increasing number of free deformation modes). Other modal representations are proposed by Staib and Duncan [86] or Cohen and Cohen [18] that similarly aim at controlling the model deformation space. Cootes *et al* [23] propose a modal representation where the deformation modes are computed from a shape training set permitting the introduction of prior information on the model shape and variations into the deformation process.

Deformations based on global Euclidean transformation are often computed with the *Iterative Closest Point* (ICP) algorithm proposed by Besl and McKay [8]. Originally, only global transformations with few DOF (such as rigid or affine transformations) have been used to restrict the amount of surface deformation. However, extensions based on more sophisticated transformations have also been proposed more recently. For instance, Feldmar and Ayache [36] have introduced locally affine transformations by combining parameterized and global deformations. Also Sederberg and Parry [85] have defined *free form deformations*, later on extended by Coquillart [24], to control the number of DOF of the global transformations[47, 4]. Champleboux [15] and Declerck *et al* [29] similarly use B-spline transformations.

3.2 Globally constrained deformation scheme : a coarse-to-fine approach

To obtain a robust and accurate reconstruction, we propose to follow a coarse-to-fine approach that can smoothly control the DOF of a surface deformation in an efficient and simple manner. The proposed method is described in [62] and can be seen as a general framework combining global and local transformations.

Indeed, our approach combines the ICP algorithm described in [8] and [97] with the deformable model framework. The ICP iteratively applies a global transformation T that minimizes a least-square criterion. This criterion corresponds to the distance of the deformed model to a set of boundary points. With the notations introduced above, the optimal transformation T satisfies:

$$T = \arg \min_{T \in \mathrm{T_{reg}}} \sum_{\mathbf{p}_i \in \mathcal{S}} \|T(\mathbf{p}_i) - (\mathbf{p}_i + \beta_i f_{\mathrm{ext}}(\mathbf{p}_i))\|^2 \tag{5}$$

where $\{f_{\mathrm{ext}}(\mathbf{p}_i)\}_i$ is the set of displacement vectors of vertices towards boundary points and $\mathrm{T_{reg}}$ is a given group of transformations with a limited number of DOF. Widely used transformation groups include rigid transformations (6 DOF), similarities (7 DOF) and affine transformations (12 DOF). For these three transformation groups, there exists a closed form solution for solving equation 5 (see [71] for details).

In equation 5 the global transformation is computed from the external forces applied on the surface. It is possible to modify the deformation scheme (equation 4) to introduce both

a global transformation and a local deformation component. Let

$$f_{\text{global}}(\mathbf{p}_i) = T(\mathbf{p}_i) - \mathbf{p}_i$$

denote a new, so called, *global force* acting on vertex $\mathbf{p}_i$ and $\lambda \in [0,1]$ be a weighting coefficient. The model deforms according to the evolution law:

$$\mathbf{p}_i^{\tau+\Delta\tau} = \mathbf{p}_i^{\tau} + (1-\gamma)(\mathbf{p}_i^{\tau} - \mathbf{p}_i^{\tau-\Delta\tau}) + \lambda\,(\alpha_i f_{\text{int}}(\mathbf{p}_i^{\tau}) + \beta_i f_{\text{ext}}(\mathbf{p}_i^{\tau})) + (1-\lambda) f_{\text{global}}(\mathbf{p}_i^{\tau}).$$

λ is called the *locality* parameter. When $\lambda = 0$, the deformation is only global and the model deforms according to the ICP framework. Conversely, if $\lambda = 1$, the model deforms as a free surface, ie with a small correlation between vertex motion. Any intermediate value of λ produces local deformations with a global constraint. This approach allows a continuous evolution from global, highly constrained, transformations towards local, free deformations. It improves the model convergence similarly to the *Graduated Non-Convexity* algorithm of Blake and Zisserman [9] by convexifying the energy functional. We usually choose affine transformations in this globally constrained deformation framework since they are very efficient to compute (closed form solution) and they are limited to 12 DOF.

In general we first proceed by using highly constrained spatial deformations to get a first rough estimate of the surface position in the dataset. By using $\lambda = 0$, we basically apply a set of global affine transformations to align the model with the dataset. Then, we proceed by iteratively increasing the locality parameter λ. This approach provides an evolutional deformation scheme based on a coarse-to-fine strategy.

The extension of globally constrained deformations to the 4D case is straightforward. To take into account of the whole time sequence, the global transformation is estimated using all instants simultaneously. However, only a geometric transformation of $\mathbb{R}^3$ is estimated to avoid an elongation of the model in the time dimension. The time discretization is always the same as the number of instants in the 4D image. The global transformation is estimated by minimizing the criterion:

$$T = \arg \min_{T \in \mathrm{T_{reg}}} \left\{ \sum_{t=0}^{n-1} \sum_{i=0}^{d-1} \| T(\mathbf{p}_{i,t}) - (\mathbf{p}_{i,t} + f_{\text{ext}}(\mathbf{p}_{i,t})) \|^2 \right\} \tag{6}$$

Solving equation 6 is numerically identical to solving equation 5. The estimated transformation is applied to all vertices simultaneously. It results in a deformation of the model at every time points simultaneously.

The globally constrained deformation scheme extends to the case of 4D models. A global deformation field $\{f_{\text{global}}(\mathbf{p}_{i,t})\}_{(i,t)}$ is estimated from the global transformation T. The globally constrained motion law of a vertex becomes:

$$\begin{aligned} \mathbf{p}_{i,t}^{\tau+\Delta\tau} \;=\; & \mathbf{p}_{i,t}^{\tau} + (1-\gamma)(\mathbf{p}_{i,t}^{\tau} - \mathbf{p}_{i,t}^{\tau-\Delta\tau}) + \\ & \lambda(\alpha_i f_{\text{int}}(\mathbf{p}_{i,t}^{\tau}) + \delta_i f_{\text{time}}(\mathbf{p}_{i,t}^{\tau}) + \beta_i f_{\text{ext}}(\mathbf{p}_{i,t}^{\tau})) + (1-\lambda) f_{\text{global}}(\mathbf{p}_{i,t}^{\tau}). \end{aligned}$$

3.3 Spatial shape constraint

To introduce more prior knowledge in the deformation process, we propose to use a reference shape of the anatomical structure to recover. During the deformation process it also ensures robustness against outliers since external forces are computed around the model current shape and therefore are more likely to attract the model towards the desired boundaries.

By slightly changing the globally constrained deformation scheme described above, we can additionally provide a shape deformation constraint. Let $\mathcal{S}$ denote a deformable surface and $\mathcal{S}'$ the surface corresponding to the reference shape (at the beginning, $\mathcal{S}'^0 = \mathcal{S}^0$). At deformation stage τ, surface $\mathcal{S}^\tau$ is deformed using the globally constrained deformation scheme but with the difference that $\mathcal{S}'^\tau$ is used instead of $\mathcal{S}^\tau$ to estimate the global transformation. Thus T^τ is the best global transformation (in the least square sense) which registers $\mathcal{S}'^\tau$ onto the deformed surface set of points

$$\{\mathbf{p}_{i,t}^\tau + \beta_i f_{\text{ext}}(\mathbf{p}_{i,t}^\tau)\}_{(i,t)}.$$

$\mathcal{S}'$ evolves according to the global transformation only:

$$\mathcal{S}'^{\tau+\Delta\tau} = T^\tau(\mathcal{S}'^\tau).$$

By composing successive global transformations (assuming T_{reg} is a group for the composition operation which is the case for rigid or affine transformations), $\mathcal{S}'^\tau$ remains identical to $\mathcal{S}'^0 = \mathcal{S}^0$ up to a global transformation. The shape force applied on the deformable surface vertices is then:

$$f_{\text{global}}(\mathbf{p}_{i,t}^\tau) = \mathbf{p}_{i,t}'^\tau. - \mathbf{p}_{i,t}^\tau$$

Therefore, the model is always attracted towards its reference shape, defined by its reference position up to a global transformation. The reference model is invariant by a rigid transformation, or any other kind of transformation used for the computation. The locality parameter allows to weight the influence of the shape constraint.

Figure 6 shows an example of a face model deformed by dragging some vertices away that automatically return to their reference position under the action of this shape constraint. In this case, an affine shape constraint is used. The different images from top to bottom and left to right show the model evolution. The last image shows the model after convergence whereas the first image shows the initial model. Due to the deformation applied and the affine transformation rescaling ability, the deformed model shape is wider than the original shape.

3.4 Regularizing forces

In addition to global constraints, model deformations are regularized through the action of the internal and the temporal forces. In the following sections, we explain the computation of these forces based on the 4D meshes geometry.

Depending on the availability of a prior shape and prior motion, internal and temporal forces can both encapsulate a weak or strong prior knowledge, as summarized in table 1.

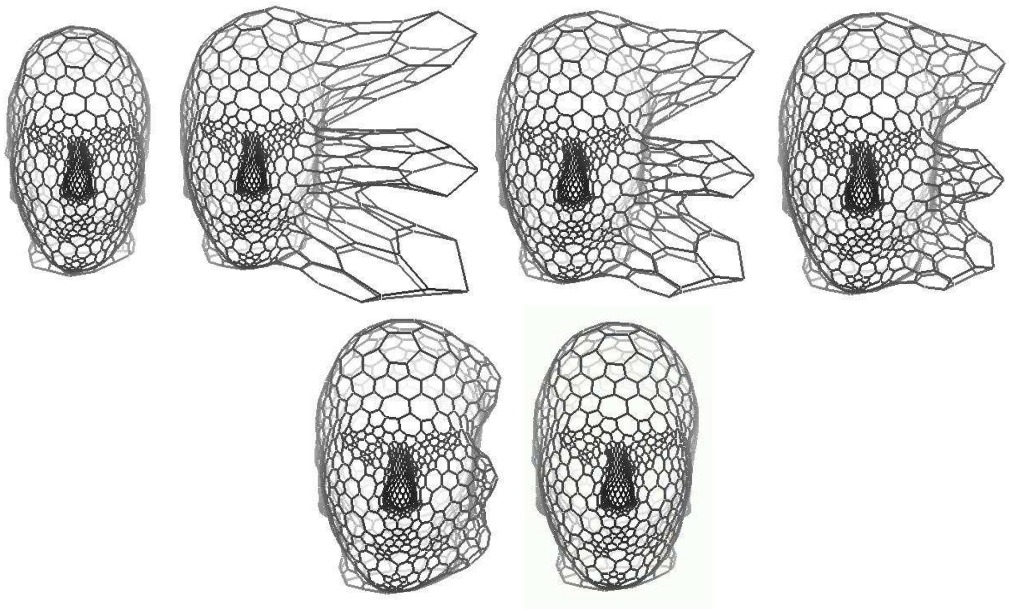

Figure 6: Convergence of a deformed model towards its reference shape under the action of an affine global shape constraint. From top to bottom, left to right, the model converges. The first image shows the original shape.

A prior shape information is used to regularize vertex displacements so that each vertex is locally attracted towards its reference shape. In the absence of prior shape knowledge, the model is spatially regularized using a curvature continuity-based criterion. Similarly, reference trajectories are used to constrain 4D deformations whereas temporal position averaging constraint is used in their absence.

Prior knowledge	Spatial constraint	Temporal constraint
Weak	Curvature-based shape smoothing	Temporal position averaging
Strong	Shape constraint	Trajectory constraint

Table 1: Spatial and temporal constraints depending of the amount of prior knowledge available.

3.5 Internal force computation

Due to its discrete nature, the regularization of a simplex mesh is not based on the evaluation of surface partial derivatives but on the relative position of a vertex with respect to its neighbors, i.e. in terms of metric parameters and simplex angles. More precisely, each vertex $\mathbf{p}_i$ is attracted towards a position $\tilde{\mathbf{p}}_i$ that locally maximizes a smoothness criterion. Let $\tilde{\varepsilon}_i^j$, $\tilde{\varphi}_i$ and $\tilde{\mathbf{p}}_i^{\perp}$ denote the metric parameters, the simplex angle and the projection of $\tilde{\mathbf{p}}_i$ on $\mathcal{P}_i$ respectively. The internal force can be decomposed as the sum of a tangential and normal component :

$$\begin{aligned} f_{\text{int}}(\mathbf{p}_i) &= f_{\text{tg}}(\mathbf{p}_i) + f_{\text{nr}}(\mathbf{p}_i) \\ &= (\tilde{\mathbf{p}}_i^{\perp} - \mathbf{p}_i^{\perp}) + (h(\mathbf{p}_{\text{ngh}_j(i)}, \varepsilon_i^j, \varphi_i) - h(\mathbf{p}_{\text{ngh}_j(i)}, \tilde{\varepsilon}_i^j, \tilde{\varphi}_i))\mathbf{n}_i \end{aligned}$$

where h is defined in equation 1.

The tangential component of the internal force controls the vertex spacing over the surface. To ensure uniformly spread vertices, metric parameters are all set equal : $\tilde{\varepsilon}_i^1 = \tilde{\varepsilon}_i^2 = \tilde{\varepsilon}_i^3 = \frac{1}{3}$. The normal component constrains the mean curvature of the surface through the simplex angle. The definition of $\tilde{\varphi}_i$ depends on the level of geometric regularity that should be enforced.

Let $\mathcal{N}_s(i)$ be the set of all vertices connected to the vertex of index i by a path of topological length less than s edges. The scale parameter, s, defines the neighborhood size over which the mesh is regularized and plays an important role. For medical image segmentation we usually consider either a (weak) smoothing constraint enforcing the C^2 continuity of the surface or a (strong) shape constraint.

3.5.1 Smoothing (weak spatial) constraint

To ensure that the vertex discrete mean curvature converges towards the weighted average mean curvature of its neighborhood, we set

$$\tilde{\varphi}_i = \arcsin\left(r_i \sum_{j \in \mathcal{N}_s(i)} e_{ij} \frac{\sin(\varphi_j)}{r_j} \right) \text{ with } \{e_{ij}\}_{ij} \text{ such that } \sum_{j \in \mathcal{N}_s(i)} e_{ij} = 1. \quad (7)$$

This smoothness constraint is used when no anatomical shape information is available (weak spatial constraint). The mesh submitted to only smoothing constraints converges towards a constant curvature shape: a sphere. Note that this constraint does not cause any shrinking effect contrarily to the classical snake smoothing forces [34].

3.5.2 Shape (strong spatial) constraint

Let $\{\varphi_i^\circ\}_i$ be the set of simplex angles defining the reference shape of an anatomical structure. Setting $\tilde{\varphi}_i = \varphi_i^\circ$ constrains the surface that converges towards the reference shape in the absence of external forces. This constraint should be used when prior shape information is available, which is usually the case. Similarly to what is done in the smoothing constraint case, a scale parameter s can be introduced that controls the spatial extension of the shape constraint at a local scale over the mesh [61].

3.6 Temporal forces computation

Similarly to internal forces ensuring a spatial regularity of the model, temporal forces are used with 4D models to ensure a geometric continuity over time. More precisely, under the action of this temporal force, a vertex $\mathbf{p}_{i,t}$ is attracted towards a point $\tilde{\mathbf{p}}_{i,t}$ lying on an optimal trajectory :

$$f_{\text{time}}(\mathbf{p}_{i,t}) = \tilde{\mathbf{p}}_{i,t} - \mathbf{p}_{i,t}.$$

Once again, we propose two kinds of temporal regularizing behaviors.

3.6.1 Smoothing (weak temporal) constraint

A vertex at time t is attracted towards the middle of its two temporal neighbors:

$$\tilde{\mathbf{p}}_{i,t} = \frac{\mathbf{p}_{i,t-1} + \mathbf{p}_{i,t+1}}{2}.$$

Applying this force is equivalent to minimizing the kinetic energy of the 4D model. Under the unique action of this force, all meshes within a 4D deformable model converge towards the same shape at every instant of the sequence (after convergence, $\forall i \in [0, d-1]$, $\forall t, l \in [0, n-1]^2$, $\mathbf{p}_{i,t} = \mathbf{p}_{i,l}$). If a curvature-based smoothing is used, the 4D mesh evolves towards a sphere with a constant radius through time.

If the time dimension is not periodic, all trajectories should be straight lines and the extremal points ($\{\mathbf{p}_{i,0}\}_i$ and $\{\mathbf{p}_{i,n-1}\}_i$) are not affected by any temporal regularization.

3.6.2 Trajectory (strong temporal) constraint

Spatial shape constraints are responsible for attracting the model towards its reference shape. Similarly we propose temporal shape constraints designed to drive each 4D model trajectories towards a reference trajectory in order to make use of the 4D prior motion information throughout the deformation process. To store prior trajectories, we could store the n positions $\{\mathbf{p}_{i,t}\}_{t\in[0,n-1]}$ of each vertex over time. However, this representation would imply that the trajectory orientation and scale is constant between images, which is not the case. Instead, we choose to store the 3D curve trajectory as the set of geometric parameters $\{\tilde{\varepsilon}_{i,t}, \tilde{\varphi}_{i,t}, \tilde{\psi}_{i,t}\}_{(i,t)}$ as described in section 2.4.1. These parameters are invariant to rotation, translation, and scale. The time shape force is defined through the attractive point:

$$\tilde{\mathbf{p}}_{i,t} = \tilde{\varepsilon}_{i,t}\mathbf{p}_{i,t-1} + (1-\tilde{\varepsilon}_{i,t})\mathbf{p}_{i,t+1} + g(\mathbf{p}_{i,t-1}, \mathbf{p}_{i,t+1}, \tilde{\varepsilon}_{i,t}, \tilde{\varphi}_{i,t})(\cos(\tilde{\psi}_{i,t})\mathbf{r}_{i,t} + \sin(\tilde{\psi}_{i,t})\mathbf{t}_{i,t} \wedge \mathbf{r}_{i,t}).$$

where $g = \|\mathbf{p}_{i,t} - \mathbf{p}_{i,t}^{\perp}\|$ as defined in appendix A. This force makes a 4D model evolve towards its reference motion up to a rigid transformation and a scale factor at all time points.

4 External force computation

The previous sections introduced the geometry and the evolution law of 3D and 4D deformable models. In this section we describe how to compute external forces that push vertices towards the closest structure boundary appearing in 4D images.

4.1 Volumetric image definition

A 3D image is defined as a discrete scalar function:

$$\begin{array}{rccc} I & : & \Gamma & \rightarrow & G \\ & & \mathbf{u} & \mapsto & I(\mathbf{u}) \end{array}$$

where Γ is the domain where the image is defined and G is the set of possible voxel grey values. Γ is a parallelepiped grid for most acquisition modalities. However, some rotative ultrasound probes acquire images on planes that intersect along a given rotation axis. We shall refer to Cartesian geometry for images with parallelepiped voxels and cylindrical geometry for images acquired with a rotative ultrasound probe [63].

This section introduces different methods for computing external forces from a 3D image. The basic assumption is that boundaries of anatomical structures appear in 3D images as intensity discontinuities. Differential operators such as the gradient operator are well suited to extract boundary voxels from the images. However, their response usually provide many false positives due to the presence of noise or other structures in the vicinity of the organ to segment. It is therefore necessary to introduce more prior knowledge such as the expected tissues grey level, to discriminate the desired boundary voxels from false positives.

4.2 Previous Work

Many data term have been proposed in the literature. A review is available in Cohen and Cohen [22].

4.2.1 Gradient's norm derivative

In their seminal paper, Kass *et al* [42] propose to compute the external forces as the gradient of the potential field $\|\nabla I\|^2$. By convolving the image with a Gaussian operator G_σ with a large standard deviation σ, the high gradient area is spread around boundary voxels. The width of the attraction potential is thus parameterized by σ and the external force writes as:

$$f_{\text{ext}} = \nabla(\|\nabla I \otimes G_\sigma\|^2).$$

This approach encounters several limitations. A Gaussian operator blurs the contours and tends to make them fade when σ increases. Also, the basin of attraction remains restricted in space around the boundary voxels which implies that the model has to be initialized very close from the data to converge. Moreover, the force computed is not a function of the distance to the data and when the gradient of the potential field is too high, it causes undesirable oscillations. Therefore, some authors [55] propose to remove oscillations by decreasing the weight coefficient β of the external force each time the model direction changes. Finally, this approach requires the computation of second derivatives of the image which may reveal unstable if the image is too noisy.

4.2.2 External force normalization

Cohen [20] demonstrates that due to the discrete representation of the gradient's norm derivative, the model displacement might become unstable as soon as the displacement of a vertex is greater than the dimension of a voxel. To overcome this problem, the author normalizes the external force in order to prevent too large displacements and to remain in the stability zone of the discrete problem:

$$f_{\text{ext}} = \frac{\nabla(\|\nabla I \otimes G_\sigma\|^2)}{\|\nabla(\|\nabla I \otimes G_\sigma\|^2)\|}.$$

This approach guarantees the stability and restricts the oscillations to an amplitude smaller than the voxel size. However, it also drastically reduces the model's convergence speed. In the deformation framework proposed in this paper, it is equivalent to reducing the β weighting parameter.

Cohen also proposes an additional term, the so called "balloon force", directed towards the surface normal. It makes the model inflate or deflate even in the absence of data. The idea is to balance the shrinking effect of the active contour internal force in order to decrease the model sensitivity to small responses of the gradient operator. Nevertheless, the simplex mesh formalism allows the definition of regularizing constraints without any shrinking effect.

4.2.3 Gradient force and boundary force

Many authors [31, 53, 19] use both boundary and local gradient information. The external force is then a combination of these two terms:

$$f_{\text{ext}}(\mathbf{p}) = f_{\text{gradient}}(\mathbf{p}) + f_{\text{boundary}}(\mathbf{p})$$

where f_{gradient} is derived from the same potential field as described above and f_{boundary} is attracting vertices towards their closest boundary point.

Cohen *et al* [19] use a distance map (Euclidean distance or discrete Chamfer distance) to determine the closest boundary point of each image voxel. The boundary force is thus defined as a function of the distance from a model vertex to its closest data point. The distance function may have different expressions depending on the desired convergence speed. In images where boundary information is sparse, the use of distance maps may cause the model to be attracted towards boundary points located at a large distance.

Delingette [31] propose to look for a boundary voxel on the normal direction of each surface vertex. This approach reduces the complexity of the boundary finding algorithm. To apply only deformations in the normal direction is not restrictive in terms of deformation capability and it avoids the introduction of a bias in the parameterization control through external force [33]. With this approach, external force are computed as a displacement vector from a vertex to its closest boundary voxel data and do not cause any oscillations.

4.3 External forces computation

As in [31] we compute external forces oriented towards each vertex normal directions. A boundary voxel is only searched within a given distance from a vertex position. Thus we can control the scan range of search and we can speed-up the computation by only considering a few voxels near each vertex.

To search boundary voxels along the normal direction, we use an algorithm similar to the Bresenham drawing line algorithm extended to the 3D case. The starting voxel in which the model vertex lies is first determined. All voxels intersected by the normal line within a given range are then determined. This algorithm may be applied to any kind of image geometry. In the classical case, voxels are parallelepipeds and the computation of the normal line intersections with voxels is straightforward. Other geometries may involve more costly computations. Figure 7 illustrates the line scanning algorithm in the case of Cartesian and cylindrical geometries.

To restrict the influence of outliers and the cost of the scanning algorithm, a maximal range parameter is used. This range may be computed as a fraction of the size of the structure to segment. If this size is unknown, a fraction of the image size is used. It is possible to gradually decrease the range of the line scanning algorithm as the model deformation process converges. The computation time is thus reduced and the model deformation is less sensitive to outliers since it eventually locks on the closest image boundaries.

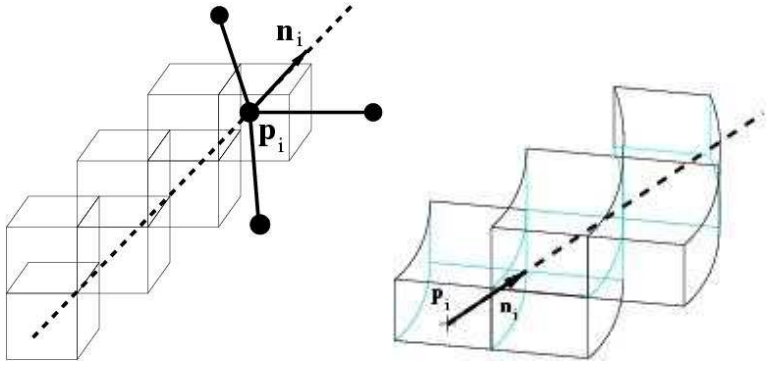

Figure 7: The line scanning algorithm extracts a discrete voxel line along the model normal direction in a Cartesian image (left) or a cylindrical image (right).

4.4 Gradient force

Gradient differential operators are the most common method to extract boundary voxels [82] from volumetric images. A common method [31, 53, 19] uses a distance map of strong contours or edge points, extracted by thresholding the response of the gradient operator. In this paper, we do not rely on these edge points or additional gradient potential force f_{gradient}. to define boundary voxels. Indeed f_{gradient} is negligible when a vertex is far from boundary points. As the vertex moves closer to the boundary, both f_{boundary} and f_{gradient} forces have the same order of magnitude and both attract the vertex towards the boundary point of minimum energy. Both terms are redundant and we found in practice that the local f_{gradient} did not improve the result convincingly.

Instead, we use the previous line scanning algorithm, the closest data point from a vertex being defined as a high gradient voxel in the normal direction. The line scanning algorithm may stop either on the first gradient voxel greater than a threshold or on the strongest gradient point in a given range. In the first case, the scheme is similar to the use of edge voxels and vertices move towards the closest boundary voxels. In the second case, no gradient threshold is required and the model converges towards the highest contrast boundaries.

Discrimination of gradient points

In many cases, voxels at a structure boundary do not necessarily always correspond to the closest boundary voxels or the highest gradient voxels. Therefore, it is necessary to find criteria that discriminate gradient voxels at the boundaries of the desired structure. First of all, a lower threshold on the gradient magnitude can be used to drop weak responses of the gradient operator. This threshold depends on the image noise level.

If the structure of interest appears to be brighter (respectively darker) than the surrounding organs all over its boundary, then the gradient vector directions is always pointing inside (respectively outside). The discrimination of boundary voxels based on the compli-

ance of their gradient orientation with the surface normal direction allows to reject many false positive contours corresponding to undesired boundaries. Since the model surface and high gradient voxels are supposed to represent the same object contour, the surface normal vectors should be roughly oriented in the same direction as the gradient vector (respectively in the opposite direction).

Finally, the intensity of the voxels in the original image gives a complementary constraint. If the intensity range of the structure to segment is known approximately, only voxels with a high enough gradient and an intensity value within a given range are considered. This information is not always helpful since high gradient voxels correspond to regions of intensity variation.

4.5 Region based forces

If the criteria proposed in the previous chapter do not allow the proper discrimination of boundary points, more prior knowledge on the structures to segment should be introduce. Liu *et al* [45] define contour detection operators robust to the image noise. Cohen *et al* [21] give a method to determine constant elevation regions (lakes) in ground numerical models. This formalism involves a lake detection operator and an energy that takes into account the deformable contour internal region (the lake) and the external region. In general, region based approaches are more discriminant than gradient based approaches [17, 81, 98]. In this section, we propose two methods to efficiently compute forces based on the constant intensity regions in the image.

Some related work on extracting homogeneous regions in case of ultrasound imaging has been proposed in the literature. Rohling *et al* [80] compound multiple acquisitions to reduce the speckle. Czerwinski [25] proposes an ultrasound speckle model. Others [11, 87] segment echocardiographic images by clustering homogeneous regions.

4.5.1 Homogeneous regions interface

The line scanning algorithm allows the extraction of intensity profiles in the image. An intensity profile at a given vertex is defined as a function of voxel intensities versus distance to the origin vertex. The left side of figure 8, shows an example of intensity profile. In the case where the image resolution is low, we perform a tri-linear interpolation of the image intensity along the normal direction for a smoother approximation of true intensity profile.

To make the force computation process less sensitive to noise, intensity values extracted may be smoothed on a small neighborhood around each point of the discrete normal segment. As the model converges towards boundary points, the model normal vectors tends to have the same direction as the gradient vector. In order to avoid blurring contours, we apply an anisotropic filtering by smoothing the image only in the tangent plane direction of each vertex. The right side of figure 8 shows an example of a neighborhood used to smooth the intensity at a given point of the intensity profile. After filtering, the intensity profile is much more regular. If the noise level is too high it is possible to increase the filtering neighborhood size at the cost of a higher computation time.

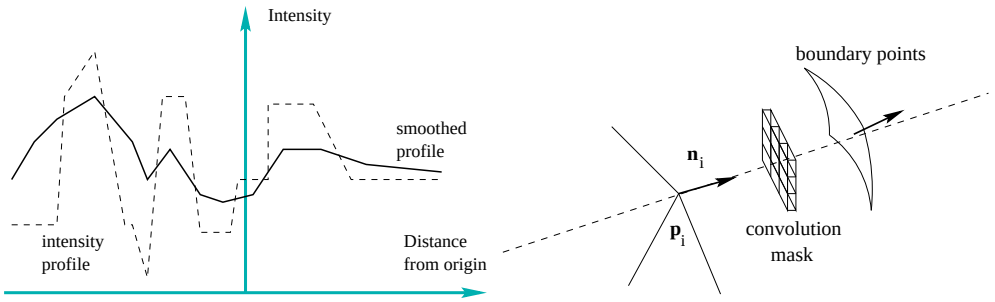

Figure 8: Left: example of an intensity profile of a 3D image along a model vertex normal direction. Right: anisotropic filter used to smooth the profile.

Homogeneous regions are defined as nearly constant intensity plateaus and therefore border between regions are located at the same distance from neighboring plateaus (see figure 9). The force applied on a model vertex is then a function of the distance from the vertex to the closest computed border.

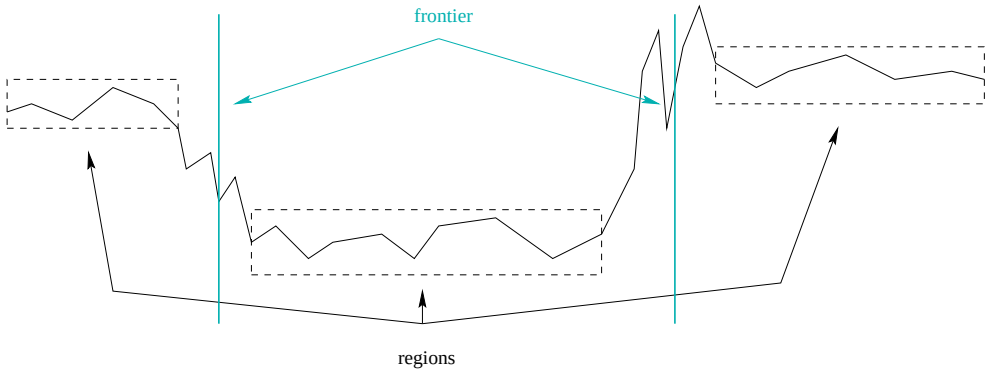

Figure 9: Definition of regions and frontiers.

This algorithm depends on several parameters:

- the external forces range;
- the size of the filtering mask;
- the minimal length of a region in terms of number of voxels ;
- the maximal intensity variation admitted around the mean plateau intensity.

These parameters allow the tuning of the algorithm to fullfill different segmentation requirements. The user is responsible for setting proper parameters depending on the properties of objects that are being recovered. It is possible to enforce the prior knowledge by indicating the intensity range for several structures composing the image.

Figure 10 shows a synthetic image segmentation example based on the use of region information. The synthetic image, on the top left image, is composed of two regions with close grey levels. The original image (I_0) is blurred by an additive Gaussian noise with standard deviation $\sigma = 5$ to produce image I_1 simulating the acquisition process noise. I_1 is in turn submitted to a multiplicative noise to produce I_2 such that:

$$I_2 = I_1 + \sqrt{I_1} G_\sigma$$

where G_σ is a 0 mean Gaussian with standard deviation $\sigma = 2$. This second filter is modelling the ultrasound noise according to experimental measurements of Loupas [48]. The top line of figure 10 shows, from left to right, the original 3D image I_0, a slice in this image, the same slice of image I_1 and of image I_2. The centre line shows the 3D image I_2, a spherical model initialized at the centre of the image, and the result of the deformation procedure by using the region criterion. Six voxels length regions with a standard deviation below 15 have been used in this experiment. Due to the model initial shape and pose, only the outer boundaries of the image are reconstructed. The curvature continuity constraint is used which results in a smoothing of the edges and corners. Figure 10 bottom line shows the intersection of the deformed surface with three orthogonal planes of the original image.

4.5.2 Regions and gradients

A different approach consists in considering the region information as a criterion to discriminate high gradient voxels. A gradient image is thus computed just as in section 4.4. Intensity profiles are extracted along each vertex normal. Since the gradient information is known, it becomes possible to perform an anisotropic filtering of the intensity profile. The profile is smoothed except in areas of high gradient to avoid breaking contours, similarly to what is done in anisotropic diffusion algorithms.

A region is still defined as a sequence of consecutive voxels with a given minimal length in a given intensity range. The high gradient voxels are used to determine structure boundaries but only gradients in the vicinity of a region border are taken into account. The force is then computed as a function of the distance from the vertex to the gradient point. In practice, it is usually sufficient to define a single region corresponding either to the structure to segment (model inner region) or to the neighboring structure (model outer region).

Figure 11 shows a new synthetic segmentation example by using contours information. The external forces are computed by looking for an internal region to the model with a given mean intensity value. The top line shows the original image, the noisy image, and the gradient's norm image. The bottom line shows the model deformation and its intersection with three orthogonal planes of the original image.

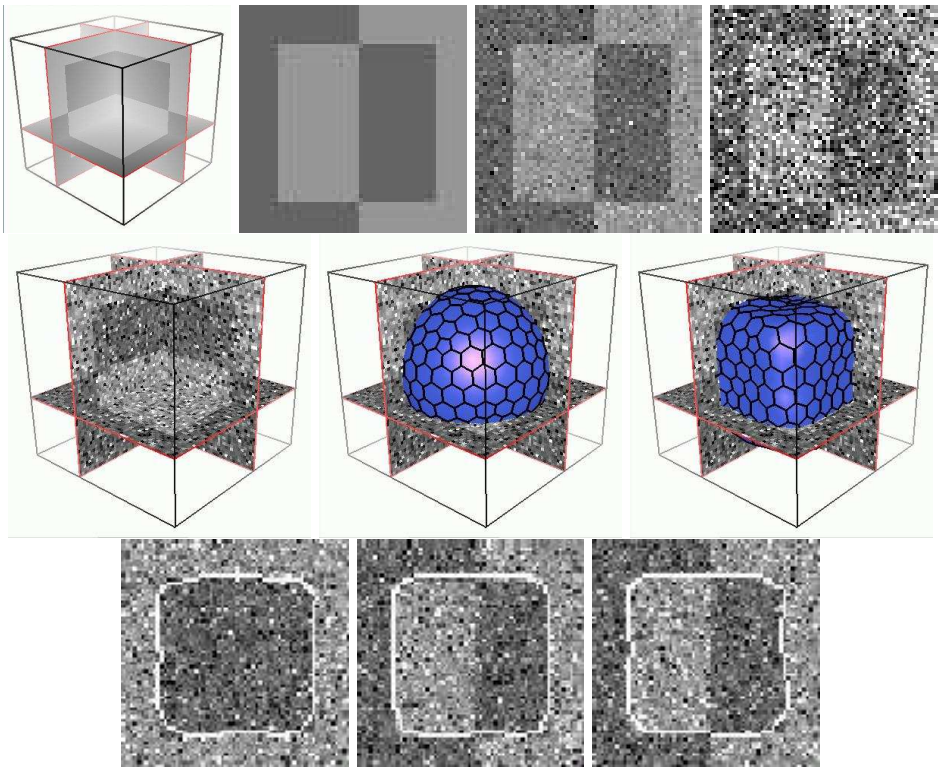

Figure 10: Top line: 3D noisy image. Middle line: model deformation in the image using a region constraint. Bottom line: intersection of the deformed model with 3 orthogonal planes of the original image.

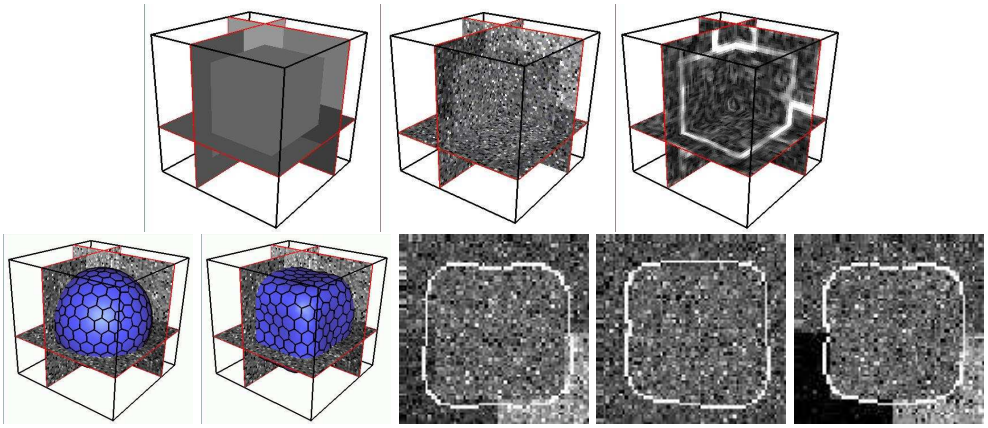

Figure 11: Top line: original 3D image, noisy image, and gradient's norm image. Bottom line: initial model, deformed model, and model intersection with three orthogonal planes of the image.

4.5.3 Discussion

The first approach does not require the image gradient computation but requires that both the inside and outside regions are known a priori. Intensity filtering only involves a neighborhood of each normal line voxel. Therefore, it uses the intensity information available in a small cylinder along the normal direction. The second approach requires high gradient voxels and only relies on a 1D filtering of the intensity profile. It is therefore more sensitive to the presence of noise. However the 1D filtering makes it very computationally efficient.

In practice, the region approaches proved to be very helpful for the segmentation of ultrasound images. Theses images show high contrast structures disturbed by the speckle. Boundaries between organs appear as thick lines that cause gradient operators to have a double response for a single boundary. Those boundaries might be considered as small regions with a high intensity on a dark background. We rely on region information coupled with model shape constraints to retrieve the meaningful image boundaries.

4.6 Intensity profile based forces

In some cases, the anatomical structures may not be characterized by very homogeneous regions because of their texture or some variable grey level surrounding organs. It is therefore necessary to introduce more appropriate prior knowledge on the data in the segmentation process. In this section we propose an intensity profile based computation method. Intensity profiles give an information on the local grey level distribution expected at the model vertices. This approach compares to iconic approaches [96, 12] based on the compliance of the grey

level distribution in two different images to perform multimodality registration. The idea is to attach a reference intensity profile to each vertex. A force is then computed that tends to locally match the reference profile with an intensity profile extracted from the image data.

4.6.1 Construction of reference intensity profiles

The use of different intensity profiles for each model vertex makes the manual construction of the profiles unpracticable. The reference intensity profiles are computed by embedding the model in a 3D image and capturing the voxel intensities along vertex normal directions. This requires to first deform the model in a reference image so that the captured profiles correspond to the intensity profiles of the structure boundaries. This prior segmentation step may involve manual editing since it only has to be done once. Thus the model carries on prior information on the shape but also on the expected grey level distribution on the boundaries of the structure for a given imaging modality for which the reference image is a representative example. An intensity profile is a set of intensity values unevenly sampled since the model normal line intersection with image voxels is irregular.

4.6.2 Similarity measures

The external force move each vertex such that its reference intensity profile matches the image voxel intensities. The algorithm computes a translation of the reference profile in the normal direction that matches a similar intensity profile extracted from the image (see figure 12).

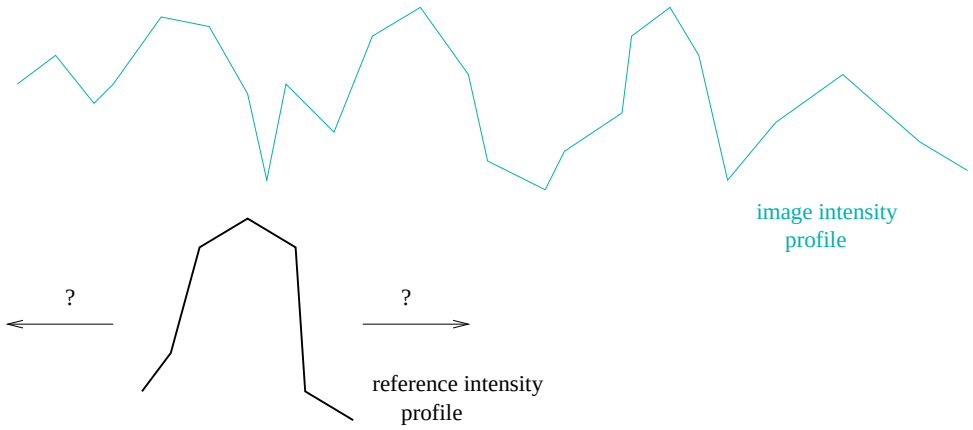

Figure 12: Registration of a reference intensity profile on an intensity profile extracted from the image along the normal direction.

The external force at a vertex is computed as the translation that best matches the two profiles. The profiles similarity measure algorithm first requires to resample both profiles with the same step. For each translation $\mathbf{t}$ of the reference intensity profile, the values of the image intensity profile are computed by linear interpolation as illustrated in figure 13. Other interpolation methods such as partial volumes [49] could be used to improve the generated values. The matching algorithm estimates the similarity of both intensity profiles exhaustively for each translation $\mathbf{t}$ using a similarity measure. The image profile sampling rate is used to determine each possible value for $\mathbf{t}$.

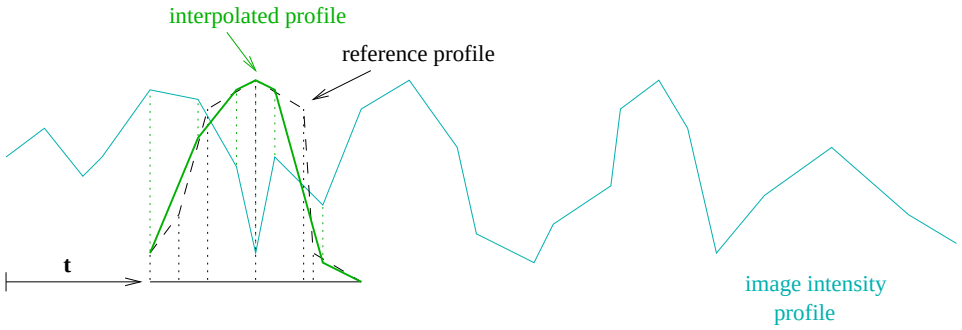

Figure 13: Linear interpolation of the reference intensity profile values to estimate the similarity with the image intensity profile.

Many similarity measures are available in literature for image registration [78, 79, 14, 72]. We experimented the sum of differences, a linear criterion, and the correlation coefficient. Let $\{v_i\}_{i\in[1,m]}$ denote the reference intensity profile set of values and $\{w_i\}_{i\in[1,m]}$ denote the corresponding image intensities. We write $\bar{v}$, $\bar{w}$, σ_v, and σ_w the means and the standard deviations of sets $\{v_i\}_i$ and $\{w_i\}_i$ respectively.

- *Differences sum.*

  This criterion defined by:

  $$C(\{v_i\}_i, \{w_i\}_i) = \frac{1}{m}\sum_{i=1}^{m} |v_i - w_i|$$

  is a simple comparison of the intensity values point by point. It is simple and robust from a statistical point of view but it only allows to compare intensity profiles coming from images with close modalities.

- *Linear criterion.*

  The criterion:

  $$C(\{v_i\}_i, \{w_i\}_i) = \frac{\left(\sum_i v_i w_i\right)^2}{\sum_i v_i^2 \sum_i w_i^2}$$

is a robust and normalized measure that makes the hypothesis of a linear transformation between $\{v_i\}_i$ and $\{w_i\}_i$ intensity values. It is normalized in interval $[0, 1]$ and its value is a similarity measure invariant by a linear transformation.

- *Correlation coefficient.*

  Similarly, the correlation coefficient:

$$C(\{v_i\}_i, \{w_i\}_i) = \frac{1}{m^2 \sigma_v^2 \sigma_w^2} \left(\sum_i (v_i - \bar{v})(w_i - \bar{w}) \right)^2$$

  is a robust and normalized measure of the correlation. It measures the intensities similarity up to an affine transformation.

4.6.3 Registration based on local similarity measures

The use of similarity measures enables to consider reference and image intensity profiles from different imaging modalities. It is therefore possible to compute a multimodality registration of the model (with profiles coming from one modality) and the image (acquired using another modality). Iconic approaches have been extensively used for multimodality registration [79, 14, 72]. It is based on the computation of similarity measures involving all image voxels. By comparison, our method adds a complementary geometric information in the registration process. Only intensities located in the area of the surface are taken into account thus avoiding outliers far from the model position. However only a few intensity values are used to estimate the similarity measure. It is therefore likely to encounter stability problems if too complex similarity measures are used. A similarity measure makes the assumption of an underlying transformation (linear, affine, etc) between the intensity profiles. The implicit computation of the transformation parameters when computing the profiles matching requires a minimal set of sampling points. Thus long enough intensity profiles have to be extracted.

Another fundamental difference between iconic registration and our approach is due to the fact that the matching is computed independently for each vertex. The algorithm estimates a large number of transformations based on the local intensity. The generated force field is then regularized through the model deformation constraints. Even if the correlation coefficient only allows to compute affine intensity transformations, different affine transformations are computed at different points in the image leading to a large ability in shape recovery.

This approach is somehow related to the work of Bouchard *et al* [10]. The authors use a geometric information acquired in the frame of a SPECT image. A laser range scanner extracts a cloud of points on a patient's face. These points are registered on the patient's face extracted from an MR or a scanner image. The geometric information is then used to register the SPECT image with the MR or scanner image.

4.7 Multimodality registration example

This section illustrates the ability of deformable models to perform multimodality registration based on intensity profiles. We use the multimodality database of Vanderbilt's University described in [93]. It is made of a set of acquisitions for several patients:

- a CT image (size: $512 \times 512 \times 28$ voxels, resolution $0,65 \times 0,65 \times 4$ mm);
- a T1 MRI image (size: $256 \times 256 \times 26$ voxels, resolution : $1,25 \times 1,25 \times 4$ mm);
- a T2 MRI (image: $256 \times 256 \times 26$ voxels, resolution : $1,25 \times 1,25 \times 4$ mm);
- a SPECT image (size: $128 \times 128 \times 15$ voxels, resolution : $2,59 \times 2,59 \times 8$ mm).

The ground truth transformation between these images is precisely computed using fiducial markers that have been later removed from the images. Figure 14 shows an example of the four modality images acquired from the same patient.

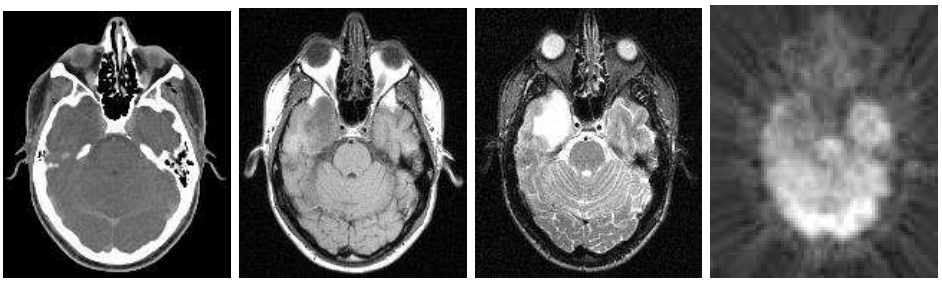

Figure 14: Slices from four modality images of a same patient. From left to right: CT image, T1 MRI, T2 MRI, and SPECT Image.

Rigid registration is computed by using surface models of the face or the inner part of the skull. The 3 similarity measures proposed above have been compared for CT-T1, T1-T2, and SPECT-T1 registration. From these experiences we can conclude that:

- The face surface model improves the registration result compared to the inner skull model. This is due to the spherical shape of the skull model in its upper part visible in the images. It gives few geometrical clues to estimate the rotation component of the rigid transformation. A geometrically representative shape is thus preferable.
- The sum of differences criterion leads to precise registration of T1 MRI with CT images. This can be explained by the similarity between the intensity values of these modalities.
- The T1-T2 and the SPECT-T1 registration require the estimation of a transformation of intensity profiles. The correlation criterion is necessary. The numerical stability

then causes problems and the intensity profiles manipulated have to be large enough (at least 30 voxels).

A quantitative study of CT-T1 registration was done. A reference model is deformed in the CT image to produce the reference model of the patient face. CT intensity profiles are extracted from the image and stored for each surface vertex. The model is then deformed under rigid constraint with $\lambda = 0$ in the MR image. A sum of differences criterion is used to compute external forces. As the model converges, the lower admissible value of the similarity measure rises to take into account only profiles with fairly matching intensities. This slows down the registration process by reducing the number of matches but this also improves the accuracy.

The top line of figure 15 shows the face model extracted from the CT image, the model embedded in the MR image, and the model after rigid registration. A rough model is good enough since we are not interested in the face modelling but in the rigid transformation estimation. The bottom lines of figure 15 show the intersection of the surface with the MR image before and after registration.

The ground truth rigid transformation $(\mathbf{R}_e, \mathbf{t}_e)$ between each CT-T1 image couple is known. The estimated rigid transformation $(\mathbf{R}, \mathbf{t})$ is compared to $(\mathbf{R}_e, \mathbf{t}_e)$ by computing the translation error (δt) and the rotation error $(\delta \mathbf{R})$ as:

$$\delta t = \|\mathbf{t}_e - \mathbf{t}\|$$

$$\delta \mathbf{R} = \mathbf{R}_e^{-1}\mathbf{R}.$$

The angle $\delta\theta$ of rotation $\delta\mathbf{R}$ is used as an intuitive measure of the rotation error. Table 2 shows the error obtained for four different patients and the resulting root mean squared (RMS) error. The RMS of a set of values $\{v_i\}_i$ equals to:

$$e = \sqrt{\frac{1}{n}\sum_i v_i^2}.$$

	$\delta\mathbf{t}$ (mm)	$\delta\theta$
patient 1	4.74	0.97
patient 2	1.18	0.76
patient 3	10.70	1.46
patient 4	1.94	1.00
RMS	5.96	1.08

Table 2: Translation and rotation registration errors

These results are compared to an accurate rigid registration method developed by Roche *et al* [77]. The results are shown for the same registration experiment by using the correlation coefficient and mutual information on all the image voxels in table 3

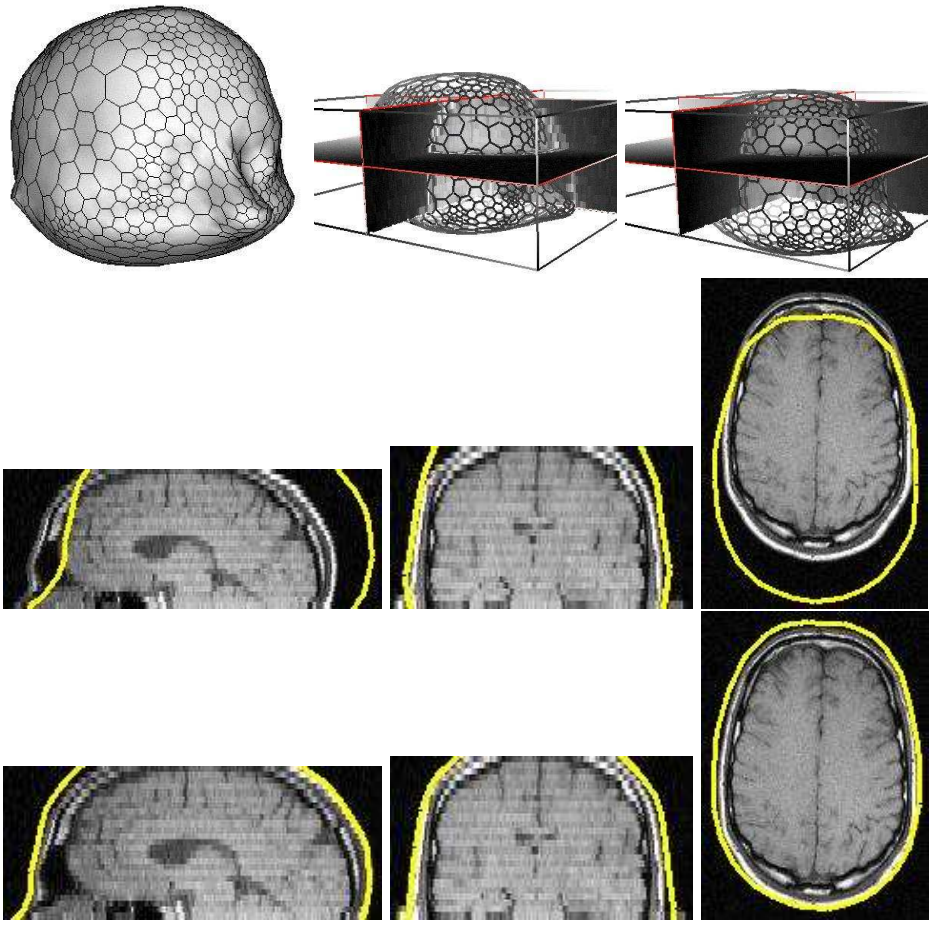

Figure 15: CT-T1 registration. Top line: face model reconstructed from the CT image, model embedded in the MR image, and model registered. Middle line: intersection of the model with 3 planes of the MR image before registration. Bottom line: intersection of the registered model with the same 3 planes after registration.

RMS	$\delta \mathbf{t}$ (mm)	$\delta\theta$
model based registration (sum of differences)	5.96	1.08
correlation coefficient	2.28	0.31
mutual information	2.19	0.58

Table 3: Comparison between model registration, correlation coefficient maximization and mutual information maximization.

This approach gives encouraging results but it has yet to be optimized to become really challenging.

5 4D medical images segmentation

4D medical images are starting to be used for cardiac dynamic studies and the monitoring of some pathologies through time. For instance, they are used to study the effect of a therapy on brain lesions growth [90, 74]. In this section, we only focus on cardiac images.

5.1 Cardiac imaging

5.1.1 Motivations

The cardiac muscle study is vital for the understanding and the early diagnosis of heart pathologies that remain the primary cause of death in western countries to date. The significant criteria for the heart pathologies detection and their therapy are the dynamic parameters of the heart motion. The heart left ventricle is the main element of the cardiac pump and it is therefore the most critical part. Heart specialists commonly use the information of heart left ventricle volume for diagnosis of heart pathologies.

The cardiac cycle is divided into two main parts: the contraction of the muscle (or systole) and the dilation (or diastole). A commonly used parameter is the ejection fraction of the left ventricle defined as the fraction of the blood volume expelled at each cardiac beat:

$$\mathrm{ef} = \frac{v_{\mathrm{dia}} - v_{\mathrm{sys}}}{v_{\mathrm{dia}}},$$

where v_{dia} is the left ventricle volume at the end of diastole and v_{sys} is its volume at the end of systole. The ejection fraction computation requires to estimate the volume at two instants of the cardiac cycle. These volumes are often roughly approximated manually from X-ray angiographies of the heart. 2D projections of the heart are acquired through a cardiac cycle and the cardiologist manually outlines the left ventricle contours on the two projections corresponding to end diastole and end systole. The ventricle volume estimate is only based on these projections.

Davis *et al* [26] study the ejection fraction of 23 patients from a slice by slice segmentation method. The mean ejection fraction is 60% with a standard deviation of 14%. The study

involves patients suffering from various cardiac troubles and shows that the ejection fraction can vary by a large amount (from 35% to 80%).

Surface models allow to estimate the heart left ventricle volume more accurately than manual or slice by slice approaches. The automation of the segmentation process and the introduction of time continuity constraints provide information on volume variations through time, without restriction to the ejection fraction alone. Figure 16 shows an example of a classical heart left ventricle volume variation through a complete cardiac cycle.

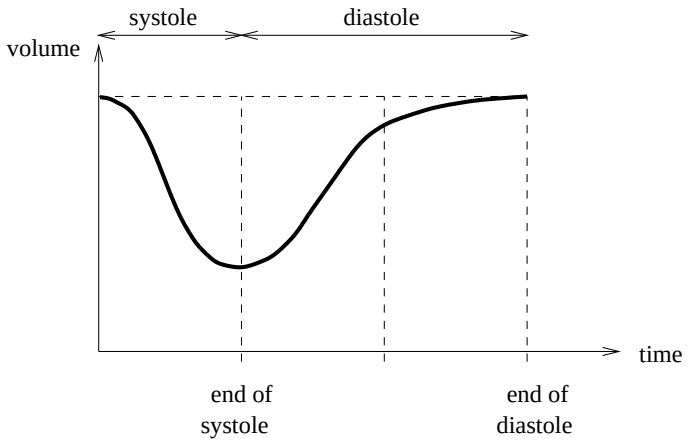

Figure 16: Volume variation of the heart left ventricle through a complete cardiac cycle.

Other quantitative parameters of cardiac dynamic may be extracted such as the septum wall thickness or the displacement of myocardium points that are representative of the cardiac muscle strength.

5.1.2 Imaging methods

Due to the cardiac beat speed, the acquisition of cardiac time sequences requires the use of fast acquisition methods. Most 3D imaging devices do not allow the real-time acquisition of a whole data volume. The acquisition is usually made plane by plane on several cardiac cycles by gating the acquisition device with the electrocardiogram (ECG) signal. Moreover, the location of the heart inside the human body makes it sensitive to breathing motion. The lack of breathing synchronization may blur the image. The 3D acquisition thus has to be realized in a time period short enough for the patient to hold his breath.

An ultrasound probe, for instance, can acquire a slice in about 20 ms. This time is short enough to neglect the cardiac motion. However, a complete cardiac volume is composed of dozens of slices. The total time is too large to enable the acquisition on a single cardiac cycle.

Figure 17 illustrates the acquisition of ECG gaited slices. To reduce the total acquisition time, slices acquisition are interlaced in time.

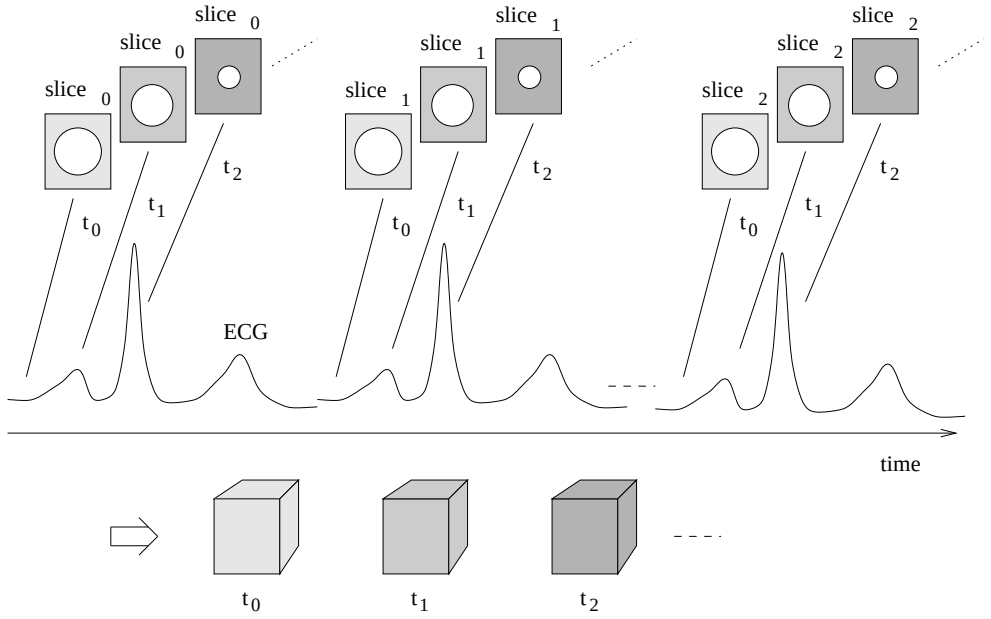

Figure 17: Acquisition of a 3D time sequence of the heart with an ultrasound probe.

All main imaging modalities allow cardiac imaging. Isotopic (SPECT) images are used for the study of the myocardium perfusion during the cardiac cycle at rest and at stress. The DSR (Dynamic Spatial Reconstructor) is an experimental scanner based on X-ray tomography method designed to acquire a volume of data in real time. MR imaging may produce synchronized slices of the heart in any orientation by using ultra-fast sequences. MRI even allows the imaging of coronaries responsible for feeding the myocardium with blood. Finally, the recent progress of 3D ultrasound (US) lead to cheap and accessible acquisition devices.

5.1.3 Images quality

In the following sections we demonstrate several segmentation experiments on MR, SPECT and US images. Due to real time imaging constraints, all 4D images have a sparse resolution. Cardiac MR images have a very high resolution in slice planes. However, the third dimension resolution is much lower ($256 \times 256 \times 9$). SPECT images are sampled on a 64^3 voxel grid. Finally, 4D US images are acquired with a rotative probe leading to a low spatial resolution ($256 \times 256 \times 9$, with a 20 degrees angle between two slices). The US image sequences are

composed of 8 time points covering only the systole while the MR (13 time points) and the SPECT (8 time points) sequences cover the complete heart cycle.

The 4D models are made of 500 to 700 vertices per surface model. This low resolution is well suited to the images level of detail. In MR and US images, the internal wall of the left ventricle is reconstructed by a closed surface representing the internal blood volume. In the case of SPECT images, the internal and external walls of the left ventricle appear. A cup shaped surface model is then used.

5.2 Previous work

The availability of ultra-fast 3D acquisition devices and sufficient computation power to deal with the amount of data produced caused a revolution of the heart dynamic study these last few years.

5.2.1 Segmentation and contour tracking

The heart left ventricle tracking in 2D or 3D image sequences and the segmentation of cardiac images have been the motivation for many research papers. Matheny and Goldgof [51] and Schudy and Ballard [84] use surface harmonics to model the shape and motion of the heart left ventricle. Many works [41, 37, 94] are dedicated to the heart left ventricle tracking in 2D ultrasound sequences. Jacob *et al* [41] use a predictive algorithm of the displacements between two successive frames. Giachetti [37] relies on a constrained deformable contour. Gorce *et al* [38] estimate the myocardium motion using the optical flow extracted from the image sequence. Winterfeldt *et al* [94] have a statistical model of the heart left ventricle contour deformations. Berger *et al* [7] track the ventricle in 3D ultrasound images with a surface model deforming accordingly with the estimated motion in an image sequence. Boukerroui *et al* [11] use a Markovian model to segment time sequence images. Sanchez-Ortiz *et al* [83] rely both on fuzzy clustering and surface model for recovering the heart left-ventricle from ultrasound images.

McEachen and Duncan [52] segment the endocardium boundary in 2D time sequences coming from different imaging modalities. They study the heart motion by comparing consecutive contours two by two. Amini and Duncan [1] track the heart left ventricle in 2D and 3D image sequences. They extract the displacement field between successive instants and they apply a smoothing filter to regularize it. McInerney and Terzopoulos [54] segment a 3D sequence using a parameterized surface discretized through the finite element method. The sequence is reconstructed by iteratively deforming the model in each 3D image of the sequence.

Reynard *et al* [75] track tags in a tagged MRI sequence. Park *et al* [70] describe a parameterized model of the left ventricle. Model parameters are functions of the distance to the model apex which allow large model shape variations. The model deforms towards feature points extracted from tagged MRI. Young *et al* [95] segment tagged MRI. Their model follows the deformations of the tag planes semi-automatically in each slice. The feature points extracted from the tag planes are used to deform a finite element mesh. The

authors validate their method with the segmentation of a synthesized object whose motion is perfectly known. Guttman *et al* [39] extract the inner and the outer boundaries of the myocardium in tagged MR images by filling up the tag planes using mathematical morphology operators. They extract the tag planes semi-automatically using prior knowledge on their location and orientation. Guttman *et al* [40] developed visualization methods to help appreciate the heart motion.

5.2.2 Cardiac dynamic

Nastar and Ayache [66, 65] segment the heart left ventricle in 2D ultrasound and 3D SPECT images by using spring-mass models. They decompose the model on a set of vibration modes [73] and they analyze the space and time spectrum of the recovered deformations. However, they do not give any interpretation of the spectral parameters for analyzing pathologies.

Park *et al* [69] analyze the left ventricle motion from tagged MRI. They used a model parameterized by functions. The model is both deformed by forces extracted from the image boundary information and from tag planes. The surface thus follows the heart boundaries but also the physical motion of the myocardium points. The parameter functions represent the inertia centre translation, the myocardium contraction in different directions, and its torsion. Each function depends on a parameter of the relative distance from the heart base and apex. It results in a dense information set. The authors compare the parameters obtained after reconstructing a pathological case and a healthy case. They show a significant difference, especially of the endocardium contraction parameter.

Robert [76] uses a parameterized deformable model to segment the left ventricle in MR or CT images. The model is a superquadric or an hyperquadric submitted to a transformation with a restricted set of parameters. The transformation consists of a rigid component to locate the model, a pinch to represent the apex, a bending for the ventricle curvature, and a torsion around the heart long axis that corresponds to a known cardiac motion. The model deformation is computed by minimizing an energy functional depending on the surface and the transformation parameters by a Levenberg-Marquardt method. An extension to the 4D case is proposed by defining each parameter q_i of the model as a function of time. Parameters are decomposed by a Fourier analysis:

$$q_i(t) = q_i^1 + q_i^2 \cos\left(\frac{2\pi t}{T}\right) + q_i^3 \sin\left(\frac{2\pi t}{T}\right) + q_i^4 \cos\left(\frac{4\pi t}{T}\right) + q_i^5 \sin\left(\frac{4\pi t}{T}\right) + \ldots.$$

The 4D model parameters, $\{q_i^j\}_{i,j}$, are estimated by minimizing the resulting energy functional. The author gives no interpretation of the parameter variations in terms of cardiac dynamic. The use of a parameterized model with few degrees of freedom restricts the shape variations capability and makes the model volume computation difficult.

Bardinet *et al* [4, 3] also use superquadrics to represent the left ventricle. They optimize the model parameters and they estimate a free-form deformation transformation. This approach gives the surface much more shape variability than in the previous case. The

extension to 4D is done by iteratively deforming the reference model in each 3D image composing the sequence. The authors show segmentation examples in CT and SPECT images. The myocardium motion estimation is done by deforming two superellipsoid for the endocardium and the epicardium using a single free-form deformation. This approach introduces a larger reconstruction error than using different FFDs. However, it provides a single transformation for all points in space. The authors estimate the motion of physical points relying on the motion of the model points. They use a synthetic object with a known motion to show that they recover a reasonable motion approximation. They show the ability of the model to recover the torsion motion. However, the reason why the model points are submitted to this torsion is not straightforward and not explained.

Clarysse *et al* [16] analyze the motion of the left ventricle surface in sequences of CT images. They consider pre-segmented data. The surface points extracted at each instant are matched according to geometrical descriptors based on curvature [44]. The curvature index s and the amount of curvature c are defined depending on the surface main curvatures k_1 and k_2:

$$s = \frac{2}{\pi}\arctan\left(\frac{k_2 + k_1}{k_2 - k_1}\right) \qquad c = \sqrt{\frac{k_1^2 + k_2^2}{2}}.$$

The time evolution of the surface is controlled by a global shape index at the global scale and a curvature based matching algorithm of surface patches at local scale. The authors validate their approach on real and synthetic data. Synthetic data are generated from real data using spherical harmonic surfaces. Pathological behavior are simulated. The authors show that global and local criteria significantly vary from healthy to pathological cases.

Declerck *et al* [28, 27] segment the endocardium and the epicardium in isotopic images. They estimate the B-spline transformation between a set of geometrical primitives defined in a reference image and boundary points extracted from the studied image. They define a 4D planispheric transformation taking into account the continuity, and possibly the periodicity, of the time dimension. The transformation estimation algorithm relies on geometrical information (boundary points and normal vector directions) in SPECT images and on tags in tagged MRI. From the planispheric transformation parameters, three significant canonic motions of the cardiac muscle are estimated:

- the *radial motion* corresponding to a contraction coefficient of the left ventricle;
- the *elevation* corresponding to the heart inflation on the vertical axis;
- and the *apico-basal rotation* measuring the torsion of the muscle around the heart big axis.

They show that the values taken by these parameters allow to distinguish between a healthy and a pathological heart motion when the parameters are estimated based on geometrical features or image tags.

5.2.3 Discussion

Among the different methods, only tagged MR imaging allows to recover the physical motion of myocardium points through the cardiac cycle. This motion is not relevant by itself and it must be described by a limited set of parameters. The significant parameters are not well known for some pathologies.

In this report, we are concerned by several imaging modalities. In particular, the poor quality of ultrasound images makes it very difficult to recover the heart motion. We therefore focus on volume analysis of the heart ventricle through time. Some recent work by Papademetris *et al* [68, 67] aim at recovering the cardiac motion from ultrasound images. They work with pre-segmented opened chest ultrasound images of dog hearts. A linear elastic model is used to analyze the myocardium deformations from the segmentation boundaries.

5.3 MR image segmentation

Cardiac MR images have a very good resolution in the slice planes (here 256×256 voxels). However, the inter-slice distance is much lower as illustrated in figure 18 showing two slices of an MR image orthogonal to the slicing planes (the anisotropy ratio is about 8). We show a segmentation experiment on a sequence composed of 13 images each having 9 slices covering the heart left ventricle. This image has been provided courtesy of General Electric Medical Systems[1]. The cardiac MR images contrast varies between slices and the heart boundaries are not very well defined.

Figure 18: Two planes orthogonal to an MR image slice direction revealing the high image anisotropy.

A 4D model is generated by embedding a 4D ellipsoid roughly centered on the left ventricle in the image sequence. Forces are computed using the image gradient with a gradient direction constraint. Only smoothing space and temporal constraints are used since no relevant prior shape is given to the model. The local deformations are constrained by a global affine transformation. A low locality coefficient prevents the surface from being too sensitive to the lack of information in areas where the gradient filter gave weak responses. The deformation process is composed of two stages. The following table shows the value of the algorithm parameters during each stage. Parameter λ is the locality factor, s is the surface rigidity, l is the force computation range, and β and δ are the external and time force weights respectively.

[1] `http://www.ge.com/medical/`

λ	β	δ	s	l
0.1	0.5	0.1	6	10
0.4	0.1	0.1	3	8

Figure 19 shows the 4D model after it has deformed in the image sequence. The model volume variation curve is drawn in figure 20. It corresponds to a non pathological volume curve (see figure 16).

Figure 21 shows the 4D model contours superimposed in the original image. One instant out of two of the original sequence is represented in the figure columns. Each row corresponds to one of the image 9 slices. The benefit of the model regularizing constraints appears in several slices where sharp variations of the blood volume in the image cause an undersignal. On the heart base (bottom row), the bottom of the atria appears in the image.

5.4 SPECT image segmentation

We have a SPECT image database provided by Professor Goris from Stanford Medical School. Each sequence consists of eight 3D images covering the complete cardiac cycle. The systole is approximatively three instants long while the diastole takes the remaining five instants. Each 3D image is composed of 64^3 voxels acquired on a regular grid. We compare images of healthy patients with a normal endocardium blood perfusion and pathological patients with an abnormal perfusion due to some ischemic zones.

5.4.1 Building the 4D model

A reference model is built from an healthy patient image. Figure 22 shows some of the long axis (top) and short axis (bottom) slices of the reference image. The reference model is built by 3D image segmentation. A surface model is first deformed in the first image of the time sequence. A sphere is manually dragged to get the cup shape of the myocardium as it appears in SPECT images. The model is locally refined based on its curvature in order to obtain a detailed and smooth enough surface. The deformed model is then used as an initialization of the second image of the sequence and so on until the entire sequence has been segmented. For each new time instant, a similarity registration of the model first compensates for volume variations and translation. Local deformations with an affine constraint then compensate for elastic deformations.

Figure 23 shows the surface models obtained at the eighth time instant of the cardiac cycle. No temporal continuity constraint have been used to produce this sequence which have motion discontinuities.

5.4.2 Healthy patient segmentation

The 4D model built is used to segment the heart in five other 4D images of different healthy patients. Figure 24 shows on a few slices of a 4D image the intersection of the model after deformation. On the top row are 4 long axis slices at 4 different instants of the cardiac cycle. On the bottom row are 4 short axis slices at the same four instants.

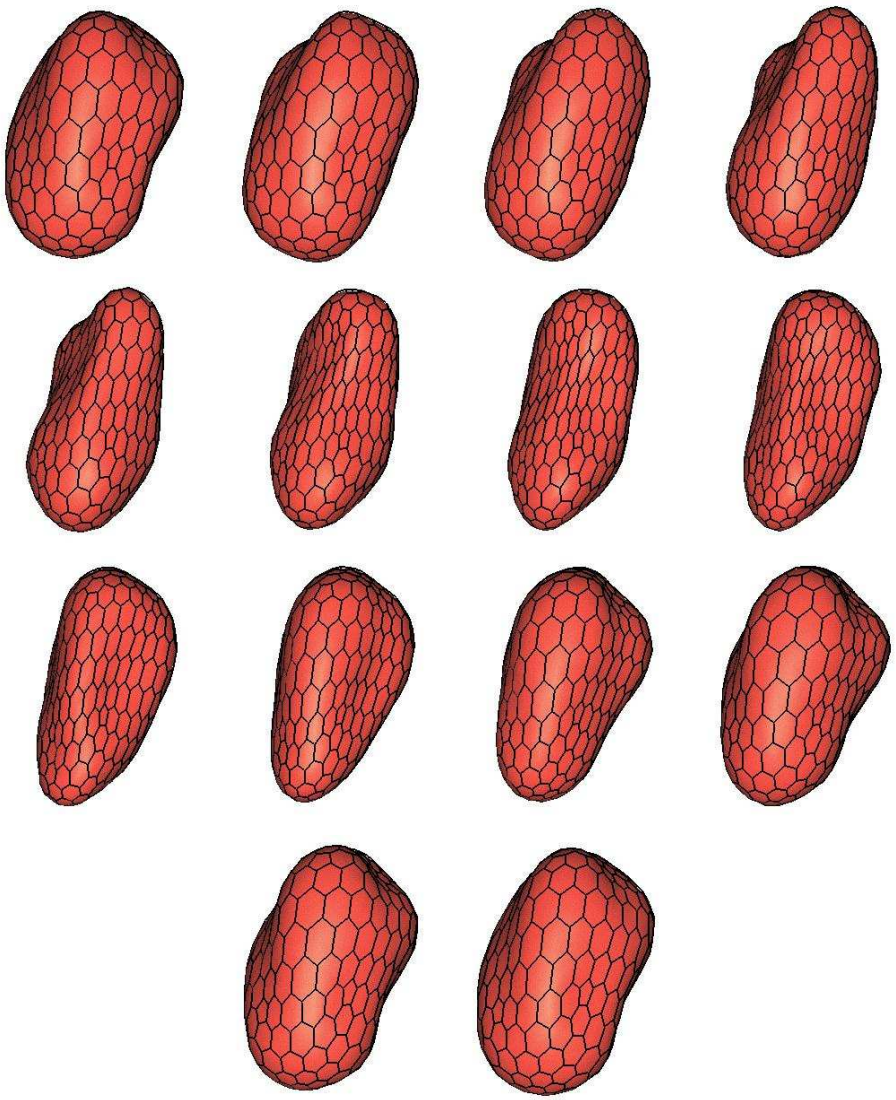

Figure 19: Heart left ventricle 4D model extracted from an MR image sequence.

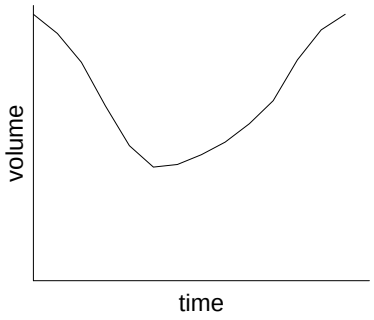

Figure 20: 4D model volume variation along the cardiac cycle.

Due to the high image contrast, gradients are used to compute external forces. The 4D model is roughly initialized in a given reference position. Rigid then similarity registration are first performed to compensate the differences in location and size between patients. Local deformations with an affine constraint are then used. By progressively increasing the locality factor and lowering the external forces range, local deformations only affect a restricted neighborhood. The gradient direction constraint is used to discriminate boundaries of the endocardium from boundaries of the epicardium. the following table shows the evolution of the deformation parameters:

λ	constraint	β	δ	s	l	number of iterations
0	rigid	1			5	35
0	similarity	1			5	15
0.2	affine	0.1	0.2	5	4	20
0.5	affine	0.1	0.2	3	2	20
0.7	affine	0.1	0.1	2	2	20

Since the original model was roughly obtained by 3D segmentation, smoothing internal constraints are used in this experiment. As can be seen on the deformed model in figure 27, the temporal smoothing constraints regularize all vertex trajectories and the deformed model motion appears much more continuous. This new model with a proper motion may be used for further segmentation using temporal shape constraints.

5.4.3 Pathological case segmentation

The segmentation of a pathological case is similar to the healthy case. Due to the poor perfusion of the myocardium in some pathologies the image contrast is much lower and the contours are weaker. The model rigidity then becomes critical for a proper reconstruction of the heart boundaries. Figure 25 shows the model intersection with 4 small short axis slices

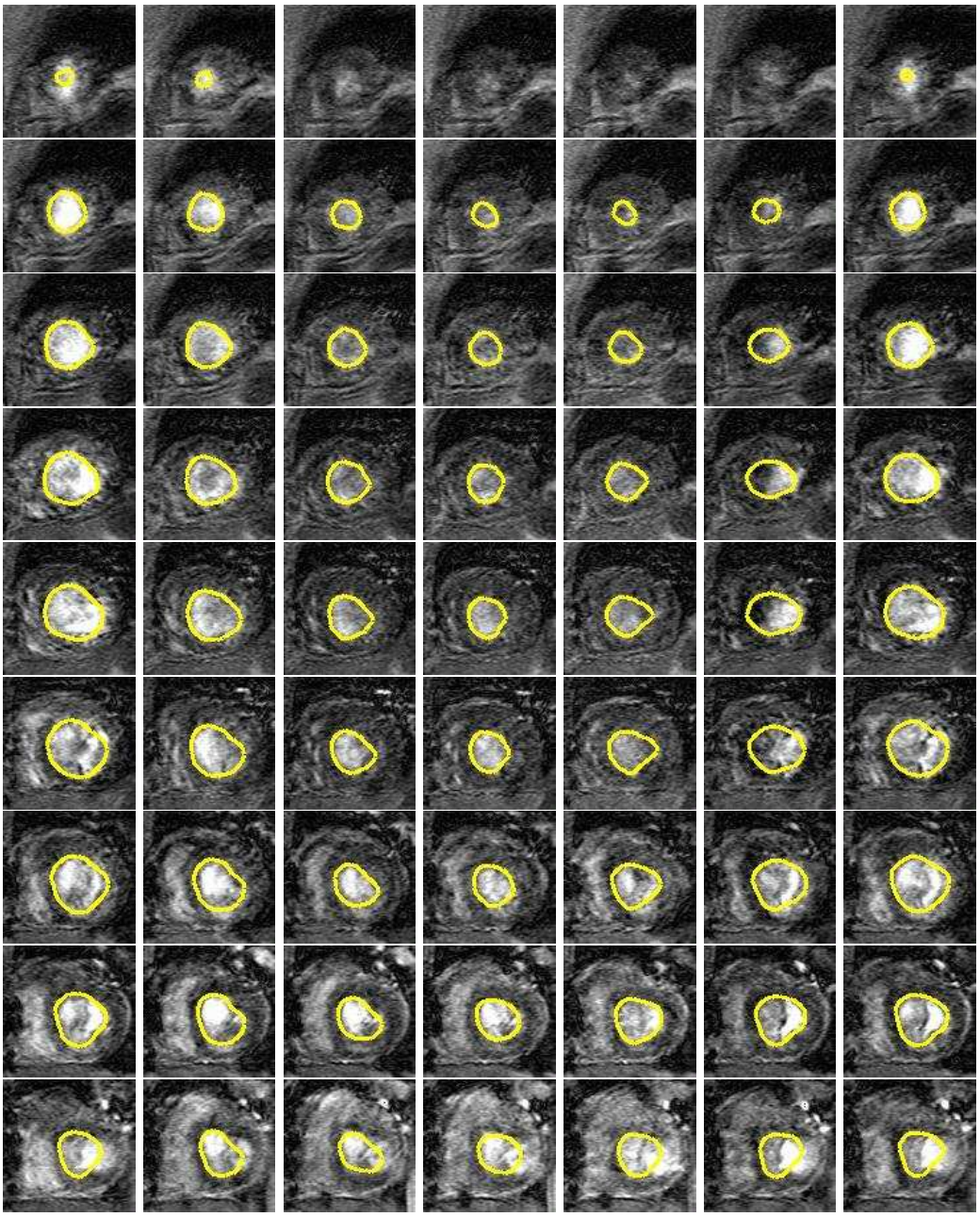

Figure 21: Reconstructed 4D model superimposed in the original MRI slices. Each line represents the time sequence of one slice of the 3D image while each column represents the set of slices composing a 3D image at one instant.

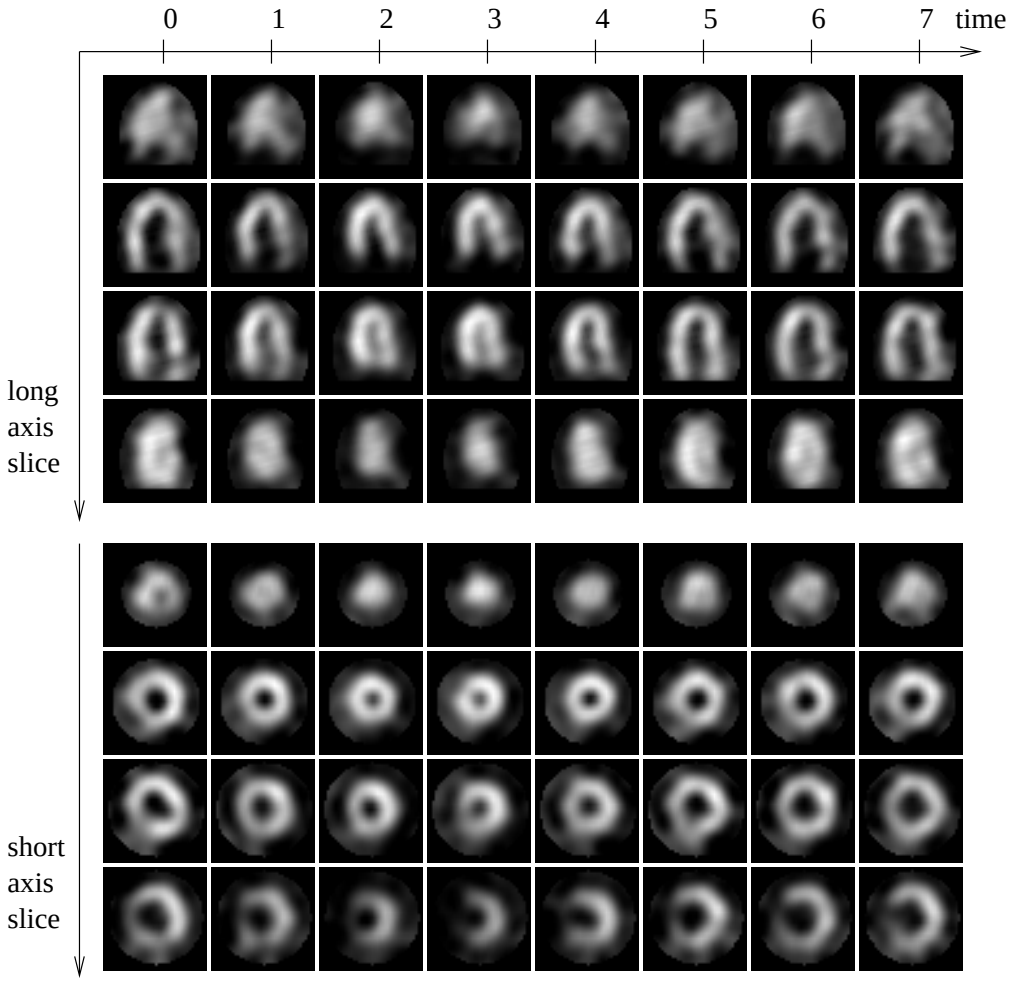

Figure 22: SPECT images used to build the 4D reference model. Top row: 4 long axis slices visualized at the height time instants. Bottom row: 4 short axis slices visualized at the 8 time instants.

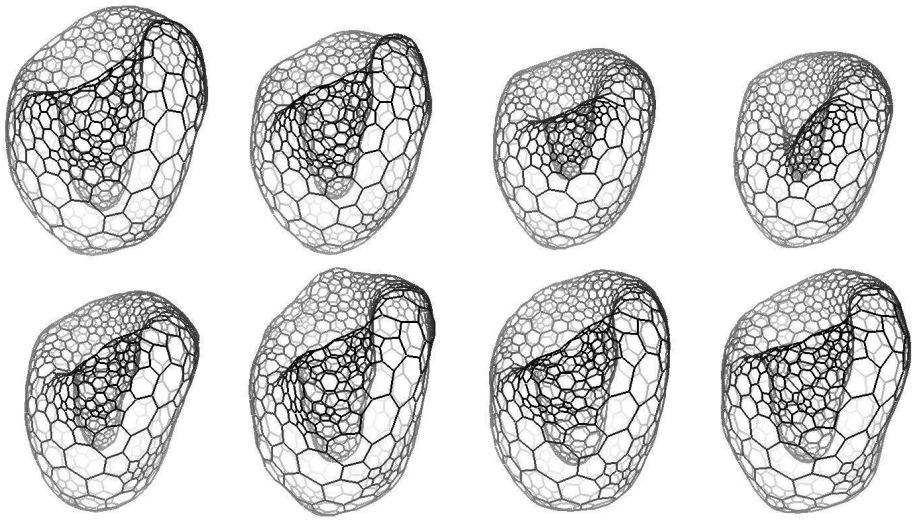

Figure 23: Eight surface models obtained by progressive deformations. The first model is obtained semi-automatically from a spherical surface. The following models are iteratively deformed in the image sequence.

and 4 long axis slices. Figure 26 shows the intersection of the model with the same slices of the gradient norm image. The shape prior information of the model allows us to reconstruct an accurate approximation of regions where no gradient response is available such as the heart apex. A segmentation error appears in the 41^{th} long axis slice around apex. The model is dragged towards a false positive gradient voxel on the heart right ventricle while left ventricle contours are lacking. It is possible to raise the model constraints to make it less sensitive to such local deformations. However it would lead to a more approximative segmentation of the remaining parts of the ventricle. The apparent error on the 20^{th} long axis slice is due to the partial volume effect. The model intersects the plane in the middle of voxels in an area where the left ventricle boundary is tangent to the image slices. This results in an apparent model shift.

5.4.4 Results

Figure 27 shows a coronal view (on the 3 top rows) and a frontal view (on the 3 bottom rows) of the 4D models. In each view appears the reference model (top), an healthy patient model (centre) and a pathological patient model (bottom).

The deformed models in 4D shows a much more regular aspect than the reference model obtained by 3D segmentation. The time periodicity clearly appears between the first and the last instant for the 4D deformed models (centre and bottom line). 4D segmentation

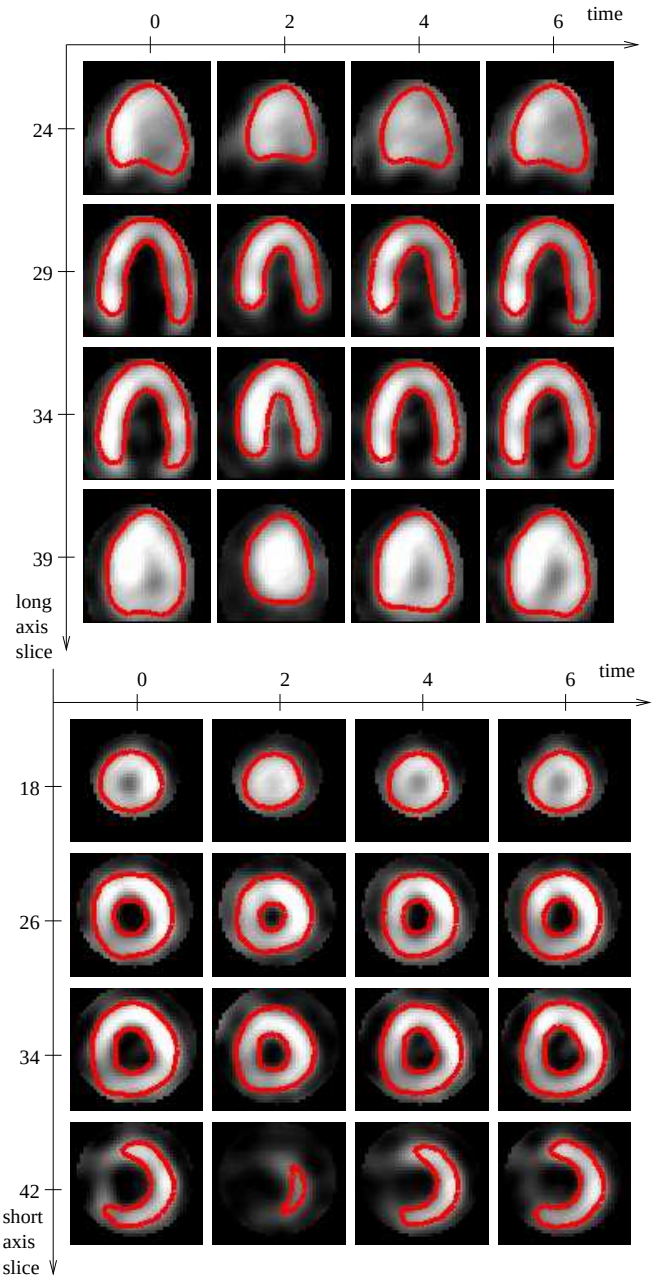

Figure 24: Segmentation example of an healthy patient. Only half of the eight instants are shown. Top row : long axis slices superimposed with the 4D model intersections. Bottom row: short axis slices superimposed with the 4D model intersections.

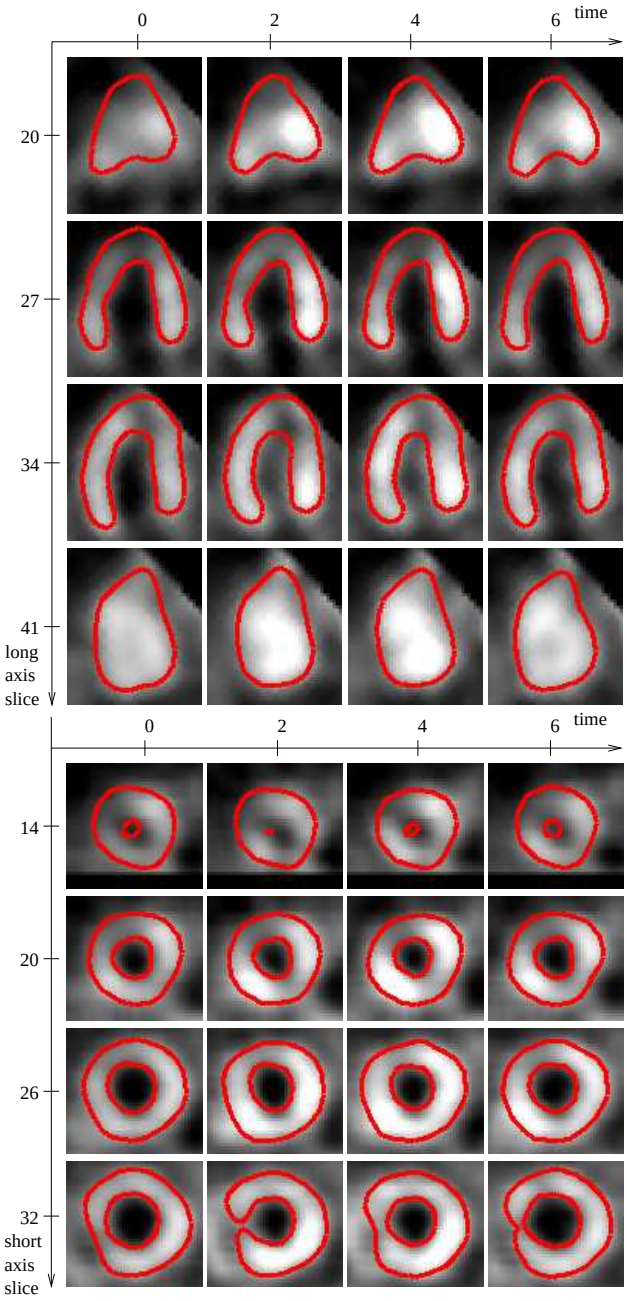

Figure 25: Pathological case segmentation. Only half of the eight instants are shown. Top row: long axis slices of the left ventricle superimposed with the model intersections. Bottom row: short axis slices superimposed with the model intersections.

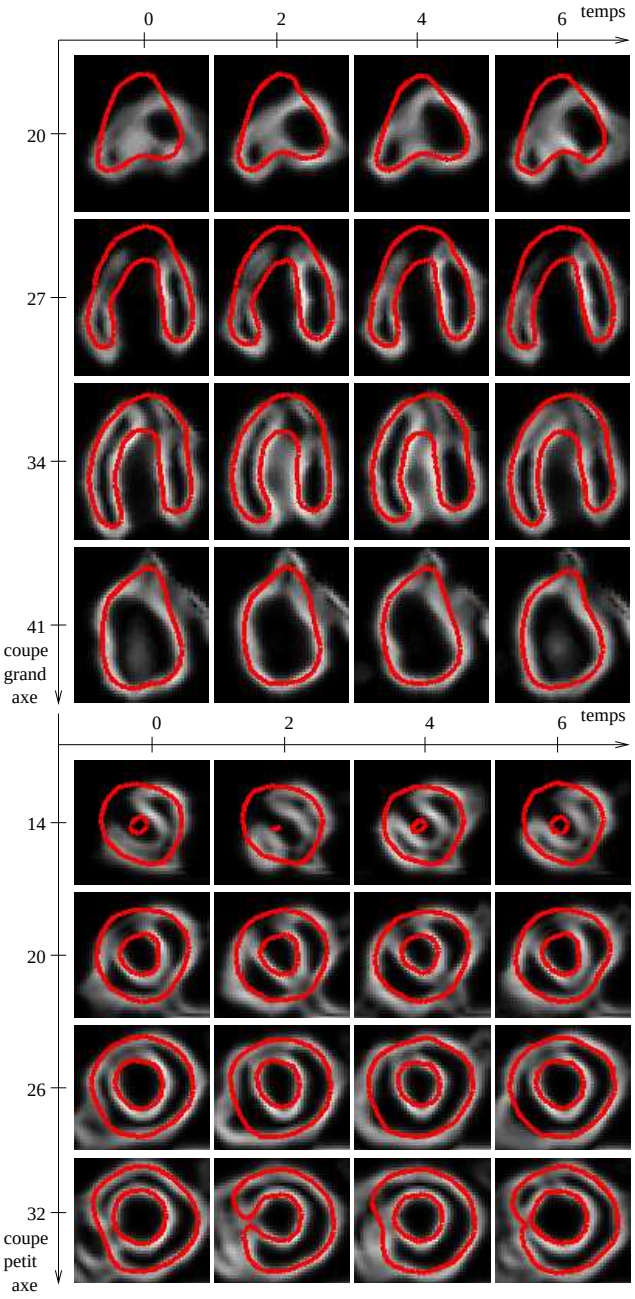

Figure 26: Intersection of the 4D model with the gradient norm image in the same slices than figure 25.

improves the recovered shape. The motion amplitude difference between the healthy and the pathological cases clearly appears on the reconstructed surfaces.

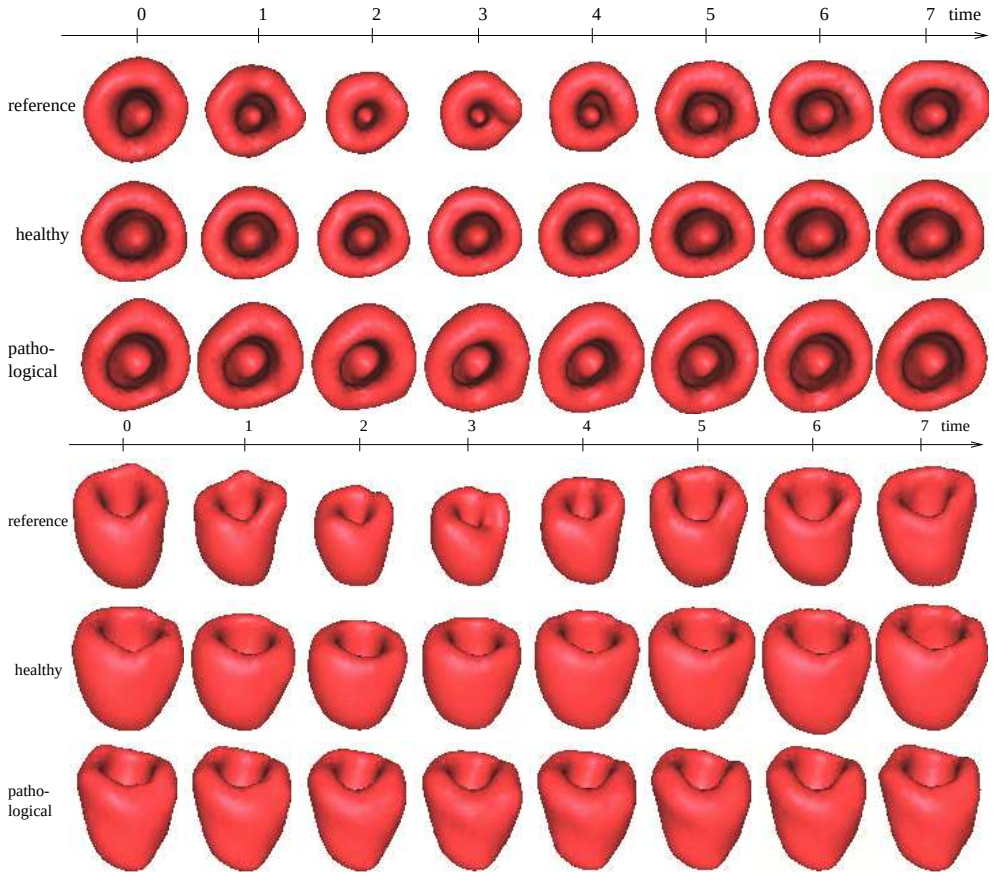

Figure 27: 4D models of the myocardium. Twice, from row to row: reference model obtained by 3D segmentation (top), healthy case (centre), and pathological case (bottom).

5.5 Ultrasound image segmentation

The speckle of ultrasound images and the lack of beam reflection on boundaries tangent to the ultrasound rays make the segmentation process difficult. 3D ultrasound images are made of a limited number of slices that only give a partial information on the acquired volume. Moreover, the acquisition of 4D images impose to reduce even more spatial resolution. We give two segmentation examples on image acquired using different ultrasound probes in this

section, showing the segmentation feasibility using shape constraints even in such difficult images.

5.5.1 First probe

A 4D model is used to make a new segmentation of the heart left ventricle in an ultrasound image acquired in CHU Barbois by Dr Lethor[2]. The image is composed of eight images acquired during the diastole. Each 3D image is acquired by a rotative probe producing a cylindrical image. Nine planes with a 20 degrees of arc spatial resolution compose a 3D image. Thus, the data is very sparse, especially away from the image axis.

Similarly to the isotopic segmentation example, the reference model is built by iterative 3D segmentation of an ultrasound sequence. The model is roughly initialized as illustrated in figure 28. The model is first registered by a similarity to adapt its scale and position to the data. The gradient information is sufficient to drive the model deformation since it is strongly constrained. A large force range is used to find boundaries far away from the initial position. After registration, the model locally deforms with an affine global constraint. Local deformations guided by region based forces with a restricted range and a weak surface rigidity are taking place in the final stage of the segmentation.

λ	constraint	force	β	δ	s	l	number of iterations
0	similarity	gradient	1		5	20	5
0.1	affine	gradient	0.5	0.1	5	20	5
1.0	affine	region	0.6	0.1	5	20	10

Due to the approximative shape of the model a temporal smoothing constraint is used.

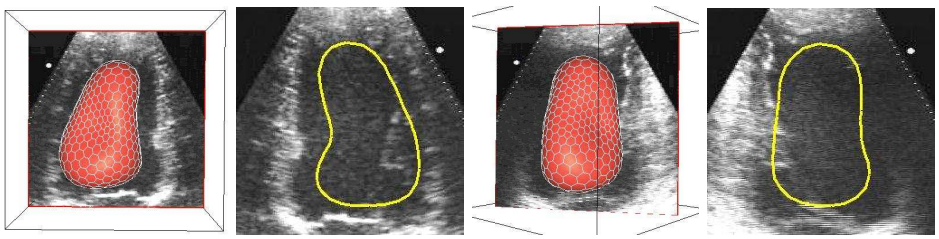

Figure 28: Model initialization inside the ultrasound image sequence. Left: surface model superimposed in the first sequence image and intersection with an image slice. Right: surface model superimposed to another slice and intersection with this slice.

Figures 29 and 30 show the deformed surface model. Figure 29 represents the model with the same viewpoint at each instant. The poor resolution of the images enables the use an a rough initial model. The apex round shape is due to the lack of information in the top

[2] `http://www.loria.fr/~berger/echocard.html`

of image (see figure 32). Figure 30 shows the transparent model superimposed to one of the image slice through the sequence.

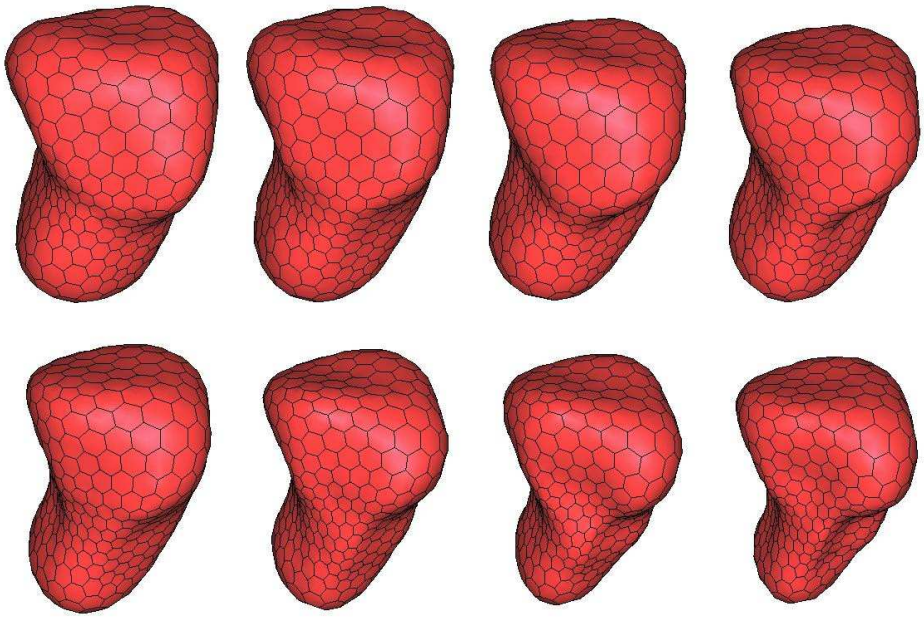

Figure 29: Deformed model in the ultrasound image sequence.

Figure 31 shows the temporal evolution of the heart left ventricle (solid line) volume. These results are compared to the one obtained by an iterative 3D segmentation of the same sequence (dashed line) from an earlier study [63]. The temporal regularizing constraints smoothes the volume evolution of the 4D model. The initial volume value in both methods are very close (3% difference) but the difference in volume estimation increases over time. This is not surprising since the 3D segmentation tends to accumulate errors. Moreover, the 4D curve shows a profile closer from the theoretical line expected (see figure 16). The model volume leads to a 49% ejection fraction. This value compares favourably to the ejection fraction computed from a manual segmentation by a cardiologist on the same sequence (45%).

Figure 32 shows all sequence slices with the superimposed surface model intersections. The 8 figure columns correspond to the 8 instants. The 9 rows correspond to each plane of the image (from top to bottom: 0, 20, 40, 60, 80, 100, 120, 140, and 160 degrees of arc slice). The regularizing constraints effect appears in several slices where the contour does not seem to follow the visible boundaries. Indeed, the contours of rows 3, 4 and 5 in second row are explained by the contours of the slices in the same columns (spatial continuity) and

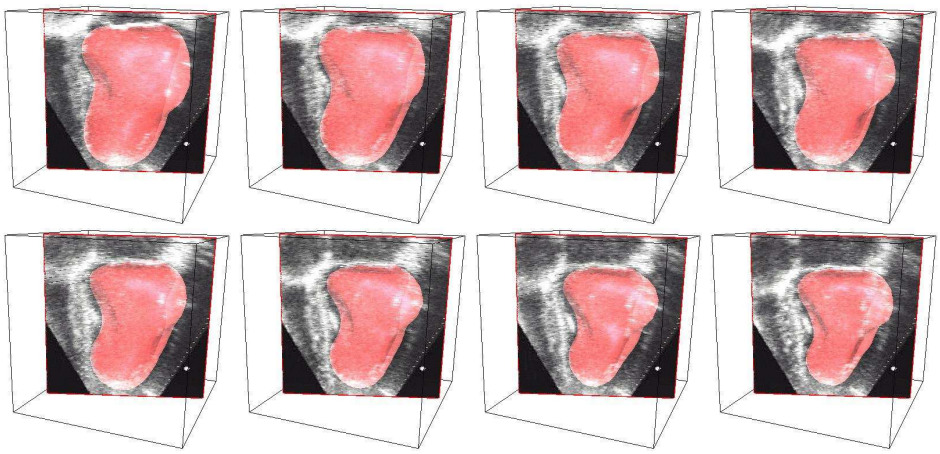

Figure 30: Transparent model overlaid on one of the image slices.

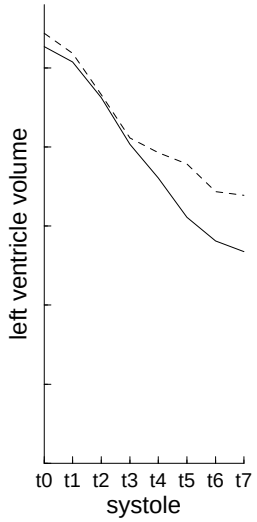

Figure 31: Heart left ventricle volume evolution in the sequence 8 instants. Solid line: 4D model volume. Dashed line: cascading 3D models volume.

by the contours of the column 2 and 6 slices (time continuity). Due to the location of the ventricle boundaries on the border of the image, the cylindrical geometry is responsible for large partial volume effects.

5.5.2 Second probe

We have a few ultrasound sequences of the heart systole acquired by ATL, a Philips Medical System company. These 4D images were acquired by a trans-thoracic rotative probe. The resulting image is disturbed by some ultrasound beam occlusion of the ribs causing the apex to fully disappear in the example shown. Moreover, the image acquisition axis does not match the heart long axis. The image is difficult to interpret and its segmentation is made difficult by the sparse acquisition planes cutting the heart in the atria.

Due to these problems, only region forces and shape constraints allow a proper segmentation of the image. Thick lines clearly appear in the left ventricle lateral wall region. The model deforms towards bright external regions with small width. Temporal and shape constraints are used. The apex reconstruction is only based on the shape constraints. An affine global constraint restricts the local deformations:

λ	constraint	α	β	δ	r	l	number of iterations
0.1	similarity	1	1	0.1	5	20	8
0.1	affine	1	1	0.1	5	20	10
0.2	affine	1	1	0.1	5	20	10
0.4	affine	1	0.6	0.1	4	15	10
0.6	affine	1	0.6	0.1	4	15	10

Figure 33 shows the surface model reconstructed at 8 instants.

Figure 34 shows the deformed model superimposed with six different image slices. The rotation axis is not parallel to the heart long axis.

Figure 35 shows the model intersection with a few image slices. The columns show only half of the eight instants while the each row correspond to the six slices of figure 34.

6 Conclusion

We have demonstrated the ability of deformable surfaces to segment 3D and 4D medical images. Deformable surfaces enable the introduction of prior knowledge on the shape of anatomical structures to improve the robustness against noise and outliers of the reconstruction process. We have fully extended the framework of deformable models to 4D images by introducing temporal regularizing constraints similar to the space regularizing constraints. Trajectory constraints tend to constraint each vertex motion towards its reference trajectories (prior motion knowledge). This approach is fully 4D since spatial and temporal constraints are used at the same time to control deformations. Shape constraints are used to segment difficult images such as ultrasound images even in the presence of occlusions.

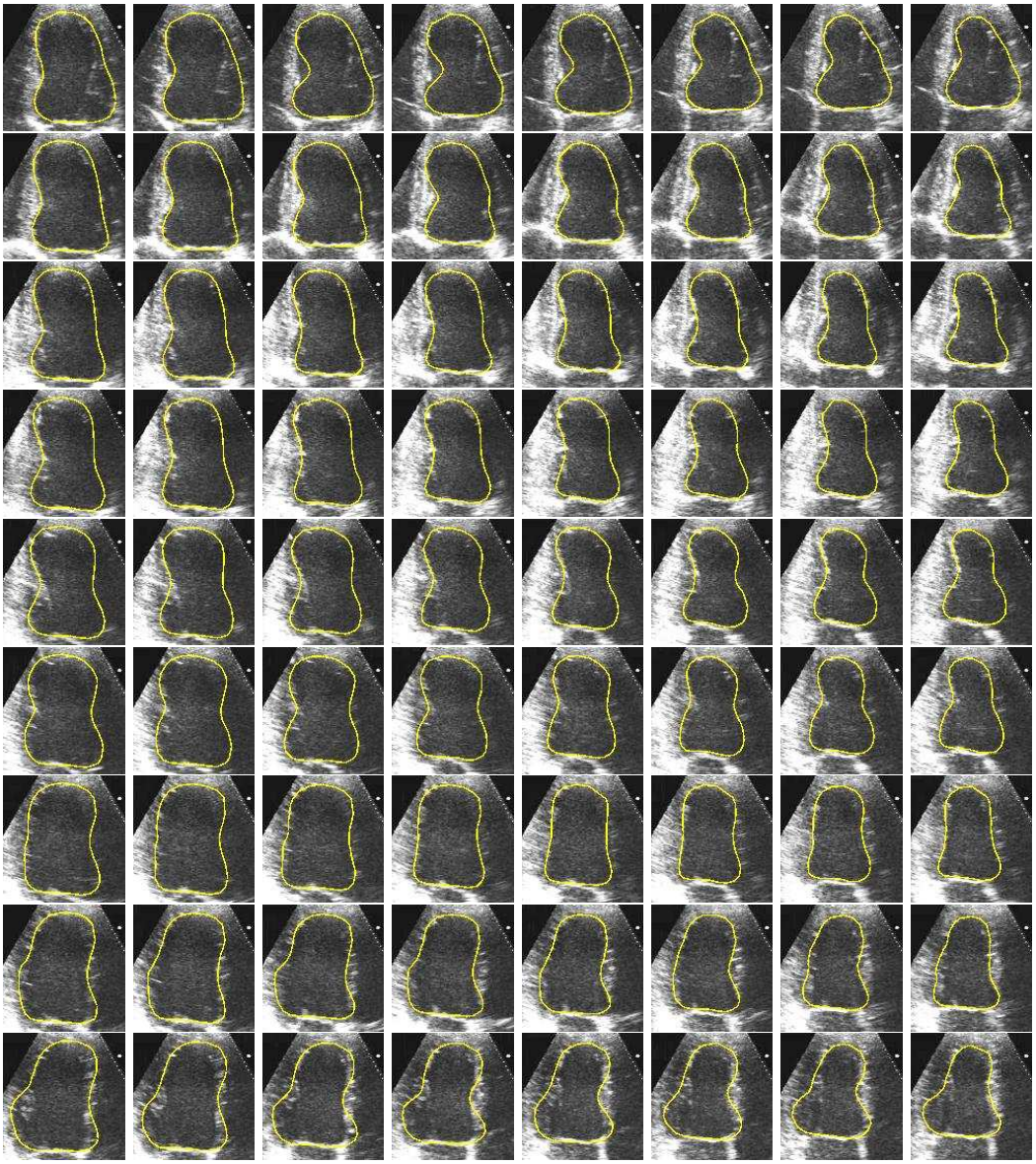

Figure 32: Set of ultrasound slices where deformed model intersections are superimposed. From left to right: cardiac sequence instant. From top to bottom: slices oriented with angle 0, 20, 40, 60, 80, 100, 120, 140, and 160 degrees of arc.

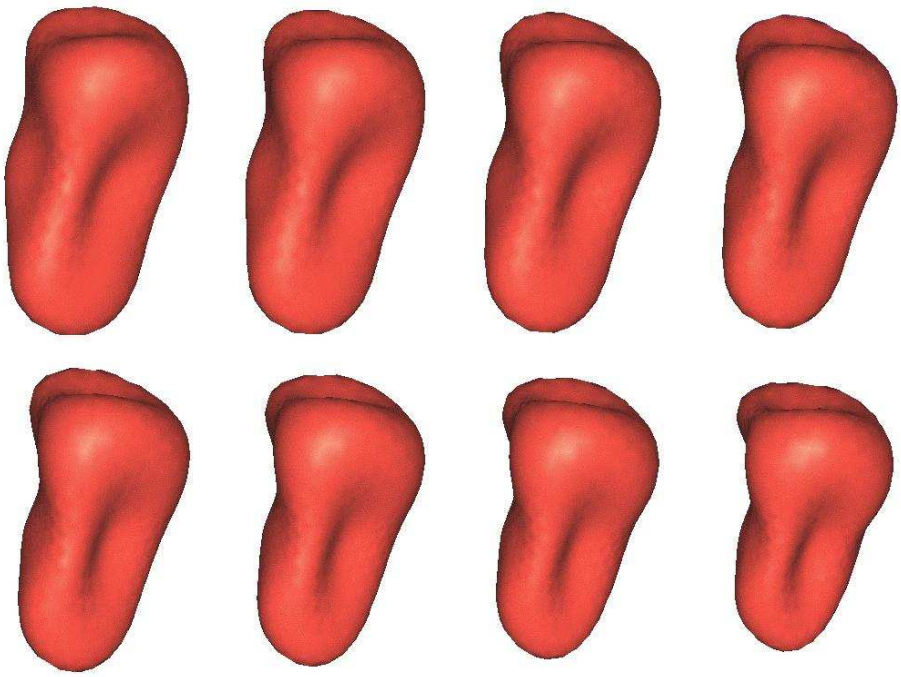

Figure 33: Surface models deformed in the ultrasound sequence.

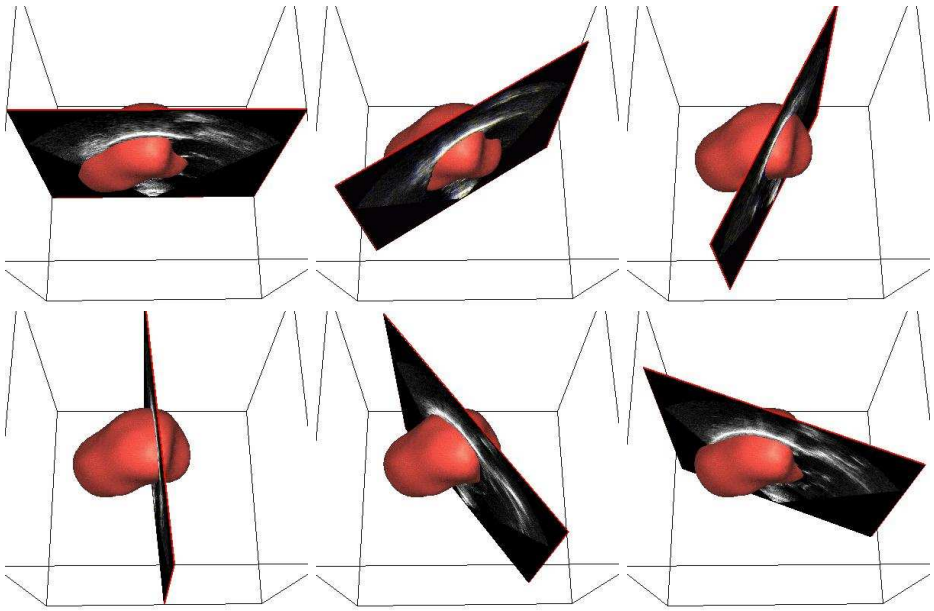

Figure 34: Deformed model superimposed in a few image slices.

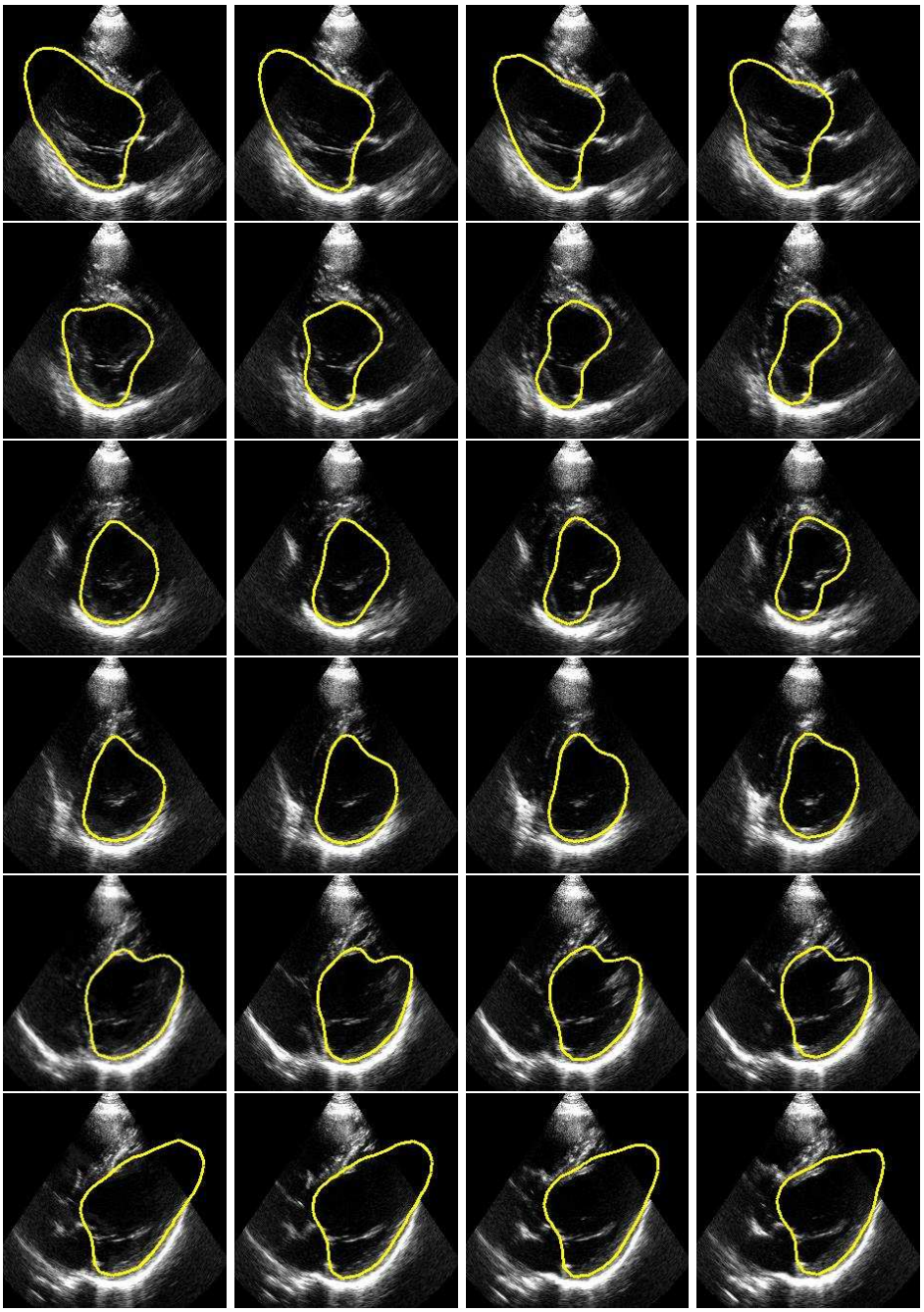

Figure 35: Ultrasound image slices with the intersections of recovered ventricle model. The horizontal direction corresponds to time while the vertical direction corresponds the different slice planes.

We propose a general purpose segmentation tool adapted to segmentation of different anatomical structures in different image modalities. The deformable models approach is also well suited to handle different image geometry. We have devised a coarse-to-fine approach based on global shape constraints that greatly contribute to control in a simple and efficient manner, the scale of the deformation. Finally, different external forces controlled by parameters such as scanning range or force weights allows us to tailor the image attraction term to different segmentation tasks.

This approach encounters limitations when the shape of the structures to segment is not known. For instance, lesions often do not have a characteristic shape and their contours are blurred in the image. It is difficult to reconstruct a satisfying geometrical representation of lesions. Complete vascular trees with complex topology and thin structures are also likely to cause problems [46]. The segmentation of very curved surfaces such as the cortex may require special forces computation to ensure the model convergence inside the gyri despite of regularizing constraints [91].

This study demonstrates the feasibility of the surface based segmentation of many medical images but a thorough validation would be required for a given clinical application. Validation is a complex problem due to the tedious and error prone manual segmentation and difficulties to compare automatic with manual segmentation results quantitatively [2, 6]. A precise validation method is to compare the model volume reconstructed on image fantoms whose size are well known. However, producing a realistic fantom of the beating heart is a complex task.

The deformable surface segmentation tool may be improved for a given clinical application by introducing more prior knowledge on the data to segment. Cootes *et al* [23] rely on shape statistical variations extracted from a training set. In case of high quality images it is possible to add topology constraints to allow changes in the model topology [57, 50, 32].

The ability to introduce hard constrains may also reveal helpful to improve segmentation results. User interaction, for instance by imposing some points where the surface should go through, is an important property of the explicit formulation of deformable models. Also, constraints on the local maxima of curvature may also prevent some unlikely deformations.

Acknowledgements

We are grateful to GE Medical Systems, for providing the 4D MRI used in this study. Thanks also go to Professor Goris of the University of Stanford Medical School for providing the SPECT images. The ultrasound images are courtesy of Dr Lethor of CHU Barbois in collaboration with the Echocard projet, and ATL, a Philips Medical System company.

Appendix A

This appendix details the computation of temporal forces with prior motion knowledge as defined in section 3.6.2. The position $\mathbf{p}_{i,t}$ of a vertex is related to the position of its temporal

neighbors and the three parameters $\varepsilon_{i,t}$, $\varphi_{i,t}$, and $\psi_{i,t}$ by equation:

$$\mathbf{p}_{i,t} = \varepsilon_{i,t}\mathbf{p}_{i,t-1} + (1-\varepsilon_{i,t})\mathbf{p}_{i,t+1} + g(\mathbf{p}_{i,t-1}, \mathbf{p}_{i,t+1}, \varepsilon_{i,t}, \varphi_{i,t})(\cos(\psi_{i,t})\mathbf{r}_{i,t} + \sin(\psi_{i,t})\mathbf{t}_{i,t} \wedge \mathbf{r}_{i,t}),$$

where $g = \|\mathbf{p}_{i,t} - \mathbf{p}_{i,t}^{\perp}\|$ is the height of $\mathbf{p}_{i,t}$ above segment $[\mathbf{p}_{i,t-1}, \mathbf{p}_{i,t+1}]$ (refer to figures 5 for an illustration of the geometric parameters composing a trajectory).

The height g is estimated according to three different cases as shown in figure 36 representing a local projection of the trajectory in plane $(\mathbf{p}_{i,t-1}, \mathbf{p}_{i,t}, \mathbf{p}_{i,t+1})$. In each case, the elevation angle is defined differently.

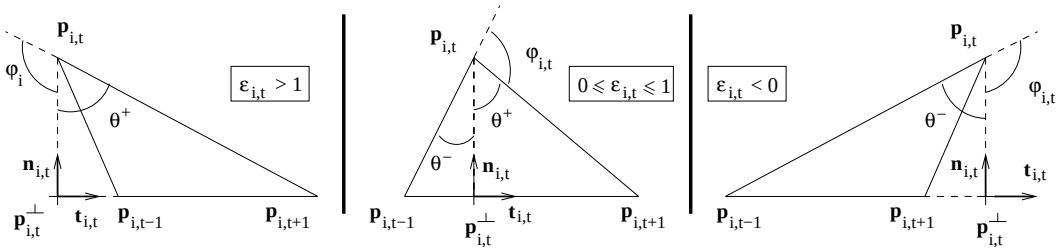

Figure 36: Three possible cases for determining the position of a point relatively to its neighbors.

Let us define the following angles: $\theta^+ = \angle \mathbf{p}_{i,t}^{\perp}\mathbf{p}_{i,t}\mathbf{p}_{i,t+1}$ and $\theta^- = \angle \mathbf{p}_{i,t-1}\mathbf{p}_{i,t}\mathbf{p}_{i,t}^{\perp}$.

- **First case :** $\varepsilon_{i,t} > 1$

  The elevation angle equals to $\varphi_{i,t} = \pi - \theta^+$, thus

  $$\tan(\varphi_{i,t}) = -\tan(\theta^+) = -\frac{\|\mathbf{p}_{i,t}^{\perp} - \mathbf{p}_{i,t+1}\|}{g}$$

  with:

  $$\|\mathbf{p}_{i,t}^{\perp} - \mathbf{p}_{i,t+1}\| = |\varepsilon_{i,t}|\|\mathbf{p}_{i,t+1} - \mathbf{p}_{i,t-1}\|$$

  thus:

  $$g(\varepsilon_{i,t}, \varphi_{i,t}, \mathbf{p}_{i,t+1}, \mathbf{p}_{i,t-1}) = \frac{-\varepsilon_{i,t}\|\mathbf{p}_{i,t+1} - \mathbf{p}_{i,t-1}\|}{\tan(\varphi_{i,t})}.$$

- **Second case :** $0 \leq \varepsilon_{i,t} \leq 1$

  In that case, the equality $\varphi_{i,t} = \pi - \theta^+ - \theta^-$ leads to:

  $$-\tan(\varphi_{i,t}) = \tan(\theta^+ + \theta^-) = \frac{\tan(\theta^+) + \tan(\theta^-)}{1 - \tan(\theta^+)\tan(\theta^-)} = \frac{\|\mathbf{p}_{i,t+1} - \mathbf{p}_{i,t-1}\|g}{g^2 + \|\mathbf{p}_{i,t}^{\perp} - \mathbf{p}_{i,t-1}\|\|\mathbf{p}_{i,t}^{\perp} - \mathbf{p}_{i,t+1}\|}. \quad (8)$$

Equation 8 admits two values for g:

$$g = \frac{\|\mathbf{p}_{i,t+1} - \mathbf{p}_{i,t-1}\|}{2\tan(\varphi_{i,t})} \left(-1 \pm \sqrt{1 + 4\varepsilon_{i,t}(1-\varepsilon_{i,t})\tan^2(\varphi_{i,t})}\right).$$

One of those two solutions is always negative and the other one, the only acceptable, is always positive. If $\varphi_{i,t} < \frac{\pi}{2}$, the first term of g is positive and the second one has to be positive as well. Else, the second term has to be negative:

$$g(\varepsilon^1_{i,t}, \varphi_{i,t}, \mathbf{p}_{i,t+1}, \mathbf{p}_{i,t-1}) = \frac{\|\mathbf{p}_{i,t+1} - \mathbf{p}_{i,t-1}\|}{2\tan(\varphi_{i,t})} \left(-1 + \epsilon\sqrt{1 + 4\varepsilon^1_{i,t}\varepsilon^2_{i,t}\tan^2(\varphi_{i,t})}\right)$$

$$\text{where } \epsilon = \begin{cases} +1 & \text{if} \quad \varphi_{i,t} < \frac{\pi}{2} \\ -1 & \text{else} \end{cases}$$

- **Third case :** $\varepsilon_{i,t} < 0$

  The elevation angle is such that $\varphi_{i,t} = \pi - \theta^-$, thus

  $$\tan(\varphi_{i,t}) = -\tan(\theta^-) = -\frac{\|\mathbf{p}^{\perp}_{i,t} - \mathbf{p}_{i,t-1}\|}{g}$$

  with:

  $$\|\mathbf{p}^{\perp}_{i,t} - \mathbf{p}_{i,t-1}\| = |1 - \varepsilon_{i,t}|\|\mathbf{p}_{i,t+1} - \mathbf{p}_{i,t-1}\|$$

  thus:

  $$g(\varepsilon_{i,t}, \varphi_{i,t}, \mathbf{p}_{i,t+1}, \mathbf{p}_{i,t-1}) = \frac{(\varepsilon_{i,t} - 1)\|\mathbf{p}_{i,t+1} - \mathbf{p}_{i,t-1}\|}{\tan(\varphi_{i,t})}.$$

References

[1] A. Amini and J. Duncan. Bending and stretching models for LV wall motion analysis from curves and surfaces. *Image and Vision Computing*, 10(6):418–430, Aug. 1992.

[2] K. Bae, M. Giger, C.-T. Chen, and C. Khan. Automatic segmentation of liver structure in CT images. *Medical Physics*, 20(1):71–78, 1993.

[3] E. Bardinet. *Modèles déformables contraints : applications à l'imagerie cardiaque.* PhD thesis, Université Paris-IX Dauphine, France, 1995.

[4] E. Bardinet, L. Cohen, and N. Ayache. Tracking and motion analysis of the left ventricle with deformable superquadrics. *Medical Image Analysis*, 1(2):129–149, 1996.

[5] G. Behiels, D. Vandermeulen, F. Maes, P. Suetens, and P. Dewaele. Active Shape-Model Based Segmentation of Digital X-ray images. In *Medical Image Computing and Computer-Assisted Intervention (MICCAI'99)*, volume 1679 of *Lectures Notes in Computer Science*, pages 128–137, Cambridge, UK, Sept. 1999. Springer.

[6] F. Bello and A. Colchester. Measuring Global and Local Spatial Correspondence Using Information Theory. In *Medical Image Computing and Computer-Assisted Intervention (MICCAI'98)*, volume 1496 of *Lecture Notes in Computer Science*, pages 964–973, Cambridge, USA, Oct. 1998. Springer.

[7] M.-O. Berger, G. Winterfeldt, and J.-P. Lethor. Contour Tracking in Echocardiographic Sequences without Learning Stage: Application to the 3D Reconstruction of the 3D Beating Left Ventricle. In *Medical Image Computing and Computer-Assisted Intervention (MICCAI'99)*, volume 1679 of *Lectures Notes in Computer Science*, pages 508–515, Cambridge, UK, Sept. 1999. Springer.

[8] P. Besl and N. McKay. A method for registration of 3D shapes. *IEEE Transactions on Pattern Analysis and Machine Intelligence*, 14(2):239–256, Feb. 1992.

[9] A. Blake and A. Zisserman. *Visual Reconstruction.* MIT Press, 1987.

[10] V. Bouchard, P. Cinquin, L. Desbat, A. Joubert, S. Lavallée, and O. Péria. A Priori Registration of SPECT Projections and MR/CT Images for SPECT Reconstruction Improvement. In *Joint Conference on Computer Vision, Virtual Reality and Robotics in Medicine (CVRMed-MRCAS'97)*, volume 1205 of *Lectures Notes in Computer Science*, pages 491–500. Springer-Verlag, Mar. 1997.

[11] D. Boukerroui, O. Basset, A. Baskurt, and A. Noble. Segmentation of Echocardiographic Data. Multiresolution 2D and 3D Algorithm Based on Grey Level Statistics. In *Medical Image Computing and Computer-Assisted Intervention (MICCAI'99)*, volume 1679 of *Lectures Notes in Computer Science*, pages 516–523, Cambridge, UK, Sept. 1999. Springer.

[12] L. Brown. A Survey of Image Registration Techniques. *ACM Computing Surveys*, 24(4):325–376, Dec. 1992.

[13] A. Bulpitt and N. Efford. An Efficient 3D Deformable Model with a Self Optimizing Topology. In *British Machine Vision Conference*, volume 1, pages 37–46, 1995.

[14] T. Buzug and J. Weese. Voxel-Based Similarity measures for Medical Image Registration in Radiological Diagnosis and Image Guided Surgery. *Journal of Computing and Information Technology*, 6(2):165–179, 1998.

[15] G. Champleboux. *Utilisation des fonctions splines pour la mise au point d'un capteur 3D sans contact : quelques applications médicales.* PhD thesis, Université Joseph Fourier, Tim3-IMAG, Grenoble, France, July 1991.

[16] P. Clarysse, D. Friboulet, and I. Magnin. Tracking Geometrical Descriptors on 3-D Deformable Surfaces: Application to the Left-Ventricular Surface of the Heart. *IEEE Transactions on Medical Imaging*, 16(4):392–404, Aug. 1997.

[17] J.-P. Cocquerez and S. Philipp. *Analyse d'images : filtrage et segmentation.* Masson, 1995.

[18] I. Cohen and L. Cohen. Hyperquadric model for 2D and 3D data fitting. In *12th International Conference on Pattern Recognition (ICPR'94)*, pages 403–405, Jerusalem, Israel, 1994.

[19] I. Cohen, L. Cohen, and N. Ayache. Using Deformable Surfaces to Segment 3-D Images and Infer Differential Structures. *Computer Vision, Graphics, and Image Processing: Image Understanding*, 56(2):242–263, Sept. 1992.

[20] L. Cohen. On Active Contour Models and Balloons. *Computer Vision, Graphics, and Image Processing: Image Understanding*, 53(2):211–218, Mar. 1991.

[21] L. Cohen, E. Bardinet, and N. Ayache. Surface reconstruction using active contour models. Technical Report 1824, INRIA, Feb. 1993.

[22] L. Cohen and I. Cohen. Finite element methods for active contour models and balloons for 2-D and 3-D images. *IEEE Transactions on Pattern Analysis and Machine Intelligence*, 15(11):1131–1147, Nov. 1993.

[23] T. Cootes, C. Taylor, D. Cooper, and J. Graham. Active shape models, their training and application. *Computer Vision and Image Understanding*, 61(1):38–59, Jan. 1995.

[24] S. Coquillart. Extended free-form deformation: A sculpturing tool for 3D geometric modeling. *ACM Computer Graphics (SIGGRAPH'90)*, 24(4):187–196, Aug. 1990.

[25] R. N. Czerwinski. Line and boundary detection in speckle images. *IEEE Transactions on Image Processing*, 7(12):1700–1714, 1998.

[26] M. Davis, B. Rezaie, and F. Weiland. Assessment of left ventricular ejection fraction from technetium-99m-methoxy isobutyl isonitrile multiple gated radionucleide angiocardiography. *IEEE Transactions on Medical Imaging*, 12(2):189–199, June 1993.

[27] J. Declerck. *Étude de la dynamique cardiaque par analyse d'images tridimensionnelles.* PhD thesis, Université de Nice Sophia-Antipolis, France, INRIA, 1997.

[28] J. Declerck, J. Feldmar, and N. Ayache. Definition of a 4D continuous planispheric transformation for the tracking and the analysis of LV motion. *Medical Image Analysis*, 2(2):197–213, June 1998.

[29] J. Declerck, J. Feldmar, M. Goris, and F. Betting. Automatic registration and alignement on a template of cardiac stress and rest reoriented SPECT images. *IEEE Transactions on Medical Imaging*, 16(7):727–737, Dec. 1997.

[30] H. Delingette. *Modélisation, déformation et reconnaissance d'objets tridimensionnels à l'aide de maillages simplexes.* PhD thesis, École Centrale de Paris, France, July 1994.

[31] H. Delingette. General Object Reconstruction based on Simplex Meshes. *International Journal of Computer Vision*, 32(2):111–146, 1999.

[32] H. Delingette and J. Montagnat. New algorithms for controlling active contours shape and topology. In *European Conference on Computer Vision (ECCV'00)*, Dublin, Ireland, June 2000.

[33] H. Delingette and J. Montagnat. Shape and topology constraints on parametric active contours. *Submitted to Computer Vision and Image Understanding*, 2000.

[34] H. Delingette and J. Montagnat. Topology and shape constraints on parametric active contours. Technical Report 3880, INRIA, Jan. 2000.

[35] H. Delingette, G. Subsol, S. Cotin, and P. J. A craniofacial surgery testbed. Technical Report 2199, INRIA, Mar. 1992.

[36] J. Feldmar and N. Ayache. Rigid, Affine and Locally Affine Registration of Free-Form Surfaces. *International Journal of Computer Vision*, 18(2):99–119, May 1996.

[37] A. Giachetti. On-line analysis of echocardiographic image sequences. *Medical Image Analysis*, 2(3):261–284, 1998.

[38] J.-M. Gorce, D. Friboulet, and I. Magnin. Estimation of three-dimensional cardiac velocity fields: assessment of a differential method and application to three-dimensional CT data. *Medical Image Analysis*, 1(3):245–261, 1996.

[39] M. Guttman, J. Prince, and E. McVeigh. Tag and contour detection in tagged MR images of the left ventricle. *IEEE Transactions on Medical Imaging*, 13(1):74–88, Mar. 1994.

[40] M. Guttman, E. Zerhouni, and M. E. Analysis of cardiac function from MR images. *IEEE Computer Graphics and Applications*, 17(1):30–38, Jan. 1997.

[41] G. Jacob, A. Noble, M. Mulet-Parada, and A. Blake. Evaluating a robust contour tracker on echocardiographic sequences. *Medical Image Analysis*, 3(1):63–75, 1999.

[42] M. Kass, A. Witkin, and D. Terzopoulos. Snakes: Active Contour Models. *International Journal of Computer Vision*, 1:321–331, 1988.

[43] A. Kelemen, G. Székely, and G. Gerig. Three-dimensional Model-Based Segmentation of Brain MRI. In *Workshop on Biomedical Image Analysis (WBIA'98)*, pages 4–13, Santa-Barbara, USA, June 1998.

[44] J. Koenderinck and A. Van Doorn. Surface shape and curvature scales. *Image and Vision Computing*, 10(8):557–565, Oct. 1992.

[45] W. Liu, I. Magnin, and G. Gimenez. Un nouvel opérateur pour la détection de ruptures dans des signaux bruités. *Traitement du Signal*, 12(3):225–237, 1995.

[46] L. Lorigo, O. Faugeras, W. Grimson, R. Keriven, R. Kikinis, and C.-F. Westin. Co-dimension 2 Geodesic Active Contours for MRA Segmentation. In *International Conference on Information Processing in Medical Images (IPMI'99)*, volume 1613 of *Lectures Notes in Computer Science*, Visegrád, Hungary, June 1999. Springer.

[47] J. Lötjönen, P.-J. Reissman, I. Magnin, and T. Katila. Model extraction from magnetic resonance volume data using the deformable pyramid. *Medical Image Analysis*, 3(4):387–406, 1999.

[48] A. loupas. *Digital image processing for noise reduction in medical ultrasonics*. PhD thesis, University of Edinburgh, UK, 1998.

[49] F. Maes, A. Collignon, D. Vendermeulen, G. Marchal, and P. Suetens. Multimodality Image Registration by Maximization of Mutual Information. *IEEE Transactions on Medical Imaging*, 16(2):187–198, Apr. 1997.

[50] R. Malladi, J. Sethian, and B. Vemuri. Shape Modeling with Front Propagation : A Level Set Approach. *IEEE Transactions on Pattern Analysis and Machine Intelligence*, 17(2):158–174, 1995.

[51] A. Matheny and D. Goldgof. The use of three- and four-dimensional surface harmonics for rigid and non-rigid shape recovery and representation. *IEEE Transactions on Pattern Analysis and Machine Intelligence*, 17(10):967–978, Oct. 1995.

[52] J. McEachen and J. Duncan. Shaped-base tracking of left ventricular wall motion. *IEEE Transactions on Medical Imaging*, 16(3):270–283, June 1997.

[53] T. McInerney and D. Terzopoulos. A Finite Element Model for 3D Shape Reconstruction and Nonrigid Motion Tracking. In *International Conference on Computer Vision (ICCV'93)*, pages 518–523, Berlin, Germany, May 1993.

[54] T. McInerney and D. Terzopoulos. A Dynamic Finite Element Surface Model for Segmentation and Tracking in Multidimensional Medical Images with Application to Cardiac 4D Image Analysis. *Computerized Medical Imaging and Graphics*, 19(1):69–83, 1995.

[55] T. McInerney and D. Terzopoulos. Topologically adaptable snakes. In *International Conference on Computer Vision (ICCV'95)*, pages 840–845, Cambridge, USA, June 1995.

[56] T. McInerney and D. Terzopoulos. Deformable models in medical image analysis: a survey. *Medical Image Analysis*, 1(2):91–108, 1996.

[57] T. McInerney and D. Terzopoulos. Medical Image Segmentation using Topologically Adaptable Snakes. In *Joint Conference on Computer Vision, Virtual Reality and Robotics in Medicine (CVRMed-MRCAS'97)*, volume 1205 of *Lectures Notes in Computer Science*, pages 92–100. Springer-Verlag, Mar. 1997.

[58] S. Menet, P. Saint-Marc, and G. Medioni. B-Snakes: implementation and application to stereo. In *Artificial Intelligence and Computer Vision*, pages 223–236. Elsevier Science, 1991.

[59] D. Metaxas and D. Terzopoulos. Constrained Deformable Superquadrics and nonrigid Motion Tracking. In *International Conference on Computer Vision and Pattern Recognition (CVPR'91)*, pages 337–343, Maui, Hawai, June 1991.

[60] J. Montagnat. *Modèles déformables pour la segmentation et la modélisation d'images médicales 3D et 4D.* PhD thesis, Université de Nice Sophia-Antipolis, France, INRIA, Dec. 1999.

[61] J. Montagnat and H. Delingette. Volumetric Medical Images Segmentation using Shape Constrained Deformable Models. In *Joint Conference on Computer Vision, Virtual Reality and Robotics in Medicine (CVRMed-MRCAS'97)*, volume 1205 of *Lectures Notes in Computer Science*, pages 13–22. Springer-Verlag, Mar. 1997.

[62] J. Montagnat and H. Delingette. Globally constrained deformable models for 3D object reconstruction. *Signal Processing*, 71(2):173–186, Dec. 1998.

[63] J. Montagnat, H. Delingette, and G. Malandain. Cylindrical Echocardiographic Images Segmentation based on 3D Deformable Models. In *Medical Image Computing and Computer-Assisted Intervention (MICCAI'99)*, volume 1679 of *Lectures Notes in Computer Science*, pages 168–175, Cambridge, UK, Sept. 1999. Springer.

[64] J. Montagnat, H. Delingette, N. Scapel, and N. Ayache. Representation, shape, topology and evolution of deformable surfaces. Application to 3D medical image segmentation. Technical Report 3954, INRIA, May 2000.

[65] C. Nastar. *Modèles physiques déformables et modes vibratoires pour l'analyse du mouvement non-rigide dans les images multidimensionnelles.* PhD thesis, École Nationale des Ponts et Chaussées, France, 1994.

[66] C. Nastar and N. Ayache. Frequency-Based Nonrigid Motion Analysis: Application to Four Dimensional Medical Images. *IEEE Transactions on Pattern Analysis and Machine Intelligence*, 18(11):1067–1079, 1996.

[67] X. Papademetris, A. Sinuas, D. Dione, R. Constable, and J. Duncan. Estimating 3D Strain from 4D Cine-MRI and Echocardiography: In-Vivo Validation. In *Medical Image Computing and Computer-Assisted Intervention (MICCAI'00)*, volume 1935 of *Lecture Notes in Computer Science*, pages 678–687, Pittsburgh, USA, Oct. 2000. Springer.

[68] X. Papademetris, A. Sinusas, D. Dione, and J. Duncan. 3D Cardiac Deformation from Ultrasound Images. In *Medical Image Computing and Computer-Assisted Intervention (MICCAI'99)*, volume 1679 of *Lectures Notes in Computer Science*, pages 420–429, Cambridge, UK, Sept. 1999. Springer.

[69] J. Park, D. Metaxas, and L. Axel. Analysis of left ventricular motion based on volumetric deformable models and MRI-SPAMM. *Medical Image Analysis*, 1(1):53–71, July 1996.

[70] J. Park, D. Metaxas, and A. Young. Deformable models with parameter functions : application to heart-wall modeling. In *International Conference on Computer Vision and Pattern Recognition (CVPR'94)*, pages 437–442, Seattle, USA, June 1994.

[71] X. Pennec. *L'incertitude dans les Problèmes de Reconnaissance et de Recalage. Application en Imagerie Médicale et Biologie Moléculaire*. PhD thesis, École Polytechnique, France, 1996.

[72] G. Penney, J. Weese, J. Little, P. Desmedt, D. Hill, and D. Hawkes. A Comparison of Similarity Measures for Use in 2D-3D Medical Image Registration. In *Medical Image Computing and Computer-Assisted Intervention (MICCAI'98)*, volume 1496 of *Lecture Notes in Computer Science*, pages 1153–1161, Cambridge, USA, Oct. 1998. Springer.

[73] A. Pentland and S. Sclaroff. Closed-Form Solutions for Physically Based Shape Modeling and Recognition. *IEEE Transactions on Pattern Analysis and Machine Intelligence*, 13(7):715–729, July 1991.

[74] D. Rey, G. Subsol, H. Delingette, and N. Ayache. Automatic Detection and Segmentation of Evolving Processes in 3D Medical Images: Application to Multiple Sclerosis. In *International Conference on Information Processing in Medical Images (IPMI'99)*, volume 1613 of *Lectures Notes in Computer Science*, pages 154–167, Visegrád, Hungary, June 1999. Springer.

[75] D. Reynard, A. Blake, A. Azzawi, P. Styles, and G. Radda. Computer tracking of tagged ^{1}H MR images for motion analysis. In *International Conference on Computer Vision, Virtual Reality and Robotics in Medicine (CVRMed'95)*, volume 905 of *Lectures Notes in Computer Science*, pages 272–276. Springer-Verlag, Apr. 1995.

[76] A. Robert. *Étude de la forme et du mouvement du coeur à partir de données lacunaires.* PhD thesis, École Nationale Supérieure des Télécomunications, France, 1996.

[77] A. Roche, G. Malandain, and A. Ayache. Unifying Maximum Likelihood Approaches in Medical Image Registration. Technical Report 3741, INRIA, July 1999.

[78] A. Roche, G. Malandain, X. Pennec, and A. Ayache. Multimodal Image Registration by Maximization of the Correlation Ratio. Technical Report 3378, INRIA, Aug. 1998.

[79] A. Roche, G. Malandain, X. Pennec, and N. Ayache. The Correlation Ratio as a New Similarity Measure for Multimodal Image Registration. In *Medical Image Computing and Computer-Assisted Intervention (MICCAI'98)*, volume 1496 of *Lecture Notes in Computer Science*, pages 1115–1124, Cambridge, USA, Oct. 1998. Springer.

[80] R. Rohling, A. Gee, and L. Berman. Three-dimensional spatial compounding of ultrasound images. *Medical Image Analysis*, 1(3):177–193, 1997.

[81] R. Ronfard. Region-based strategies for active contour models. *International Journal of Computer Vision*, 13(2):229–251, 1994.

[82] A. Rosenfeld and A. Kak. *Digital picture processing.* Academic Press, 1976.

[83] G. Sanchez-Ortiz, J. Declerck, M. Mulet-Parada, and J. Noble. Automating 3D Echocardiographic Image Analysis. In *Medical Image Computing and Computer-Assisted Intervention (MICCAI'00)*, volume 1935 of *Lecture Notes in Computer Science*, pages 687–696, Pittsburgh, USA, Oct. 2000. Springer.

[84] R. Schudy and D. Ballard. A computer model for extracting moving heart surfaces from four-dimensional cardiac ultrasound images. In *International Conference on Computer Vision (ICCV'79)*, pages 366–376, 1979.

[85] T. Sederberg and S. Parry. Free-form deformation of solid geometric models. *ACM Computer Graphics (SIGGRAPH'86)*, 20(4):151–160, Aug. 1986.

[86] L. Staib and J. Duncan. Deformable Fourier models for surface finding in 3D images. In *Visualization in Biomedical Computing (VBC'92)*, pages 90–104, 1992.

[87] G. Stetten and S. Pizer. Medial-Guided Fuzzy Segmentation. In *Medical Image Computing and Computer-Assisted Intervention (MICCAI'00)*, volume 1935 of *Lecture Notes in Computer Science*, pages 226–235, Pittsburgh, USA, Oct. 2000. Springer.

[88] D. Terzopoulos and D. Metaxas. Dynamic 3D Models with Local and Global Deformations: Deformable Superquadrics. *IEEE Transactions on Pattern Analysis and Machine Intelligence*, 13(7):703–714, July 1991.

[89] D. Terzopoulos, A. Witkin, and M. Kass. Constraints on Deformable Models: Recovering 3D Shape and Nonrigid Motion. *Artificial Intelligence*, 36(1):91–123, 1988.

[90] J.-P. Thirion and G. Calmon. Deformation Analysis to Detect and Quantify Active Lesions in Three-Dimensional Medical Image Sequences. *IEEE Transactions on Medical Imaging*, 18(5):429–441, May 1999.

[91] M. Vaillant and C. Davatzikos. Finding parametric representations of the cortical sulci using an active contour model. *Medical Image Analysis*, 1(4):295–315, 1997.

[92] B. Vemuri and A. Radisavljevic. From Global to Local, a Continuum of Shape Models with Fractal. In *International Conference on Computer Vision and Pattern Recognition (CVPR'93)*, pages 307–313, New York, USA, 1993.

[93] J. West, J. Fitzpatrick, M. Wang, B. Dawant, C. Maurer, R. Kessler, R. Maciunas, C. Barillot, D. Lemoine, A. Collignon, F. Maes, P. Suetens, D. Vandermeulen, P. van den Elsen, S. Napel, T. Sumanaweera, B. Harkness, P. Hemler, D. Hill, D. Hawkes, C. Studholme, J. Maintz, M. Viergever, G. Malandain, X. Pennec, M. Noz, G. Maguire, M. Pollack, C. Pelizzari, R. Robb, D. Hanson, and R. Woods. Comparison and Evaluation of Retrospective Intermodality Brain Image Registration Techniques. *Journal of Computer Assisted Tomography*, 21:554–566, 1997.

[94] G. Winterfeldt, M. Berger, J. Lethor, and M. Handschuhmacher. Expert Model Based 3D Reconstruction of the left Ventricle Using Transthorasic Echographic Images. In *Computers in Cardiology*, Sept. 1997.

[95] A. Young, D. Kraitchman, L. Dougherty, and L. Axel. Tracking and Finite Element Analysis of Stripe Deformation in Magnetic Resonance Tagging. *IEEE Transactions on Medical Imaging*, 14(3):413–421, July 1995.

[96] Z. Zhang. Le problème de la mise en correspondance : l'état de l'art. Technical Report 2146, INRIA, Dec. 1993.

[97] Z. Zhang. Iterative point matching for registration of free-form curves and surfaces. *International Journal of Computer Vision*, 13(2):119–152, Dec. 1994.

[98] S. Zhu. Unifying snakes, region growing, and Bayes/MDL for Multi-band Image Segmentation. Technical Report 94-10, Harvard Robotics Laboratory, 1994.

Contents

Unité de recherche INRIA Sophia Antipolis
2004, route des Lucioles - B.P. 93 - 06902 Sophia Antipolis Cedex (France)

Unité de recherche INRIA Lorraine : Technopôle de Nancy-Brabois - Campus scientifique
615, rue du Jardin Botanique - B.P. 101 - 54602 Villers lès Nancy Cedex (France)
Unité de recherche INRIA Rennes : IRISA, Campus universitaire de Beaulieu - 35042 Rennes Cedex (France)
Unité de recherche INRIA Rhône-Alpes : 655, avenue de l'Europe - 38330 Montbonnot St Martin (France)
Unité de recherche INRIA Rocquencourt : Domaine de Voluceau - Rocquencourt - B.P. 105 - 78153 Le Chesnay Cedex (France)

Éditeur
INRIA - Domaine de Voluceau - Rocquencourt, B.P. 105 - 78153 Le Chesnay Cedex (France)
http://www.inria.fr
ISSN 0249-6399